Chaotic Modeling and Simulation (CMSIM) 2: 129–140, 2014

Replication of Discrete Chaos

M. U. Akhmet[1] and M. O. Fen[2]

[1] Department of Mathematics, Middle East Technical University, 06800, Ankara, Turkey
(E-mail: marat@metu.edu.tr)
[2] Department of Mathematics, Middle East Technical University, 06800, Ankara, Turkey
(E-mail: ofen@metu.edu.tr)

Abstract. Discrete dynamics is a significant instrument for chaos investigation, since the results of the theory are rigorously approved. We provide extension of chaos by implementing chaotic perturbations to exponentially stable difference equations with arbitrarily high dimensions. Our analysis is based on the Li-Yorke definition of chaos. The results are supported with the aid of simulations. Extension of intermittency is also investigated in discussion form.
Keywords: Chaos extension, Li-Yorke chaos, Generalized synchronization, Chaotic set of sequences, Intermittency.

1 Introduction

Discrete equations are popular systems to provide a wide range of chaos and important to approve the existence rigorously [1]-[6]. The first mathematical definition of chaos for one dimensional maps is introduced by Li and Yorke [1]. The concept of snap-back repellers for high dimensional discrete equations was introduced by Marotto [2]. According to the results of the paper [2], if a multi-dimensional continuously differentiable map has a snap-back repeller, then it is Li-Yorke chaotic. Li-Yorke sensitivity, which links the Li-Yorke chaos with the notion of sensitivity, is studied in [5], and generalizations of Li-Yorke chaos to mappings in Banach spaces and complete metric spaces are provided in [4]. The Smale Horseshoe map, is first studied by Smale [7] and it is an example of a diffeomorphism which is structurally stable and possesses a chaotic invariant set [6,8–10]. The horseshoe map is prominent due to its usage for the recognition of chaotic dynamics, and can arise both in discrete and continuous cases, for example in the Hénon map [11,12] and in the Duffing equation [13,14], whenever one has transverse homoclinic orbits. If one considers the famous Lorenz [15] or Van der Pol equations [16,17], we do not have mathematically strictly proven chaos of a certain type despite there have been considered significant simplifications [18]. We propose in the present paper a rigorously confirmed

Received: 27 November 2013 / Accepted: 10 February 2014
© 2014 CMSIM
ISSN 2241-0503

method for chaos extension from known chaotic discrete equations to arbitrarily high dimensional ones.

To explain the procedure of chaos extension that is mentioned in the present study, let us consider the discrete equation $u_{n+1} = L[u_n] + h_n$, where L is a linear operator with spectra inside the unit circle in the complex plane. If the sequence $\{h_n\}$ is considered as an *input* with a certain property such as boundedness, periodicity or almost periodicity, then the discrete equation produces a solution, *output*, with a similar feature, boundedness/periodicity/almost periodicity [19,20]. Taking support from this fact, it is reasonable to consider the problem that whether chaotic inputs generate chaotic outputs. In the solution of this problem, one encounters with a difficulty such that chaotic sequences are not defined clearly as in the case of former properties. In other words, the chaoticity property can not be characterized through a single function. Instead, whichever chaos type is considered, chaotic properties include *interrelation* of functions. Exclusively, in the description of chaos through period-doubling cascade, this is expressed implicitly. This is true for discrete as well as for continuous-time chaos. Under the circumstances, we are forced to handle the problem by means of a special unfamiliar way of "collection of sequences". However, formally, one can formulate the results of the paper in the old fashion as the generation of a chaotic output from a chaotic input. It will be seen better if we agree to call the chaotic sequence that one which belongs to the chaotic set.

Throughout the paper, $\mathbb{R}$ and $\mathbb{Z}$ will denote the sets of real numbers and integers, respectively.

The problem that is investigated in the present study is as follows. We consider the discrete equations

$$x_{n+1} = F(x_n), \tag{1}$$

and

$$y_{n+1} = Ay_n + f(y_n) + g(x_n), \tag{2}$$

where $n \in \mathbb{Z}$, A is a nonsingular, constant $q \times q$ real valued matrix, and the functions $F : \mathbb{R}^p \to \mathbb{R}^p$, $f : \mathbb{R}^q \to \mathbb{R}^q$ and $g : \mathbb{R}^p \to \mathbb{R}^q$ are continuous in all their arguments. We suppose that the map F admits the chaos and possesses an invariant set $\Lambda \subset \mathbb{R}^p$. Our main goal is to show that equation (2) exhibits chaotic motions.

A concept which is related to our theory of chaos extension is the generalized synchronization [21]-[24]. According to the results of [23], generalized synchronization occurs in system (1)+(2) if and only if there exist sets $B_x \subset \mathbb{R}^p$, $B_y \subset \mathbb{R}^q$ such that the criterion

(A) $\lim_{n\to\infty} \|y_n - \overline{y}_n\| = 0,$

holds, for all $(x_0, y_0), (x_0, \overline{y}_0) \in B_x \times B_y$, where $\{y_n\}$ and $\{\overline{y}_n\}$ are solutions of equation (2) with the same solution $\{x_n\}$ of (1). Taking advantage of the criterion (A), in the next section, we will show that generalized synchronization occurs in the dynamics of equation (1)+(2).

In this paper, besides the presence of generalized synchronization, we show that if equation (1) is chaotic in the sense of Li-Yorke then the same is true for (2). In other words, equation (2) preserves the chaos type of equation (1). This is the main difference between the papers [23,24] and the present one. Moreover, we will show by examples, the convenience of our method to equations which possess intermittency and Neimark-Sacker bifurcation resulting in a stable closed curve.

2 Preliminaries

Let us describe the ingredients of Li-Yorke chaos [1]-[4]. Consider a set of uniformly bounded sequences

$$\mathscr{B} = \left\{ \{\eta_n\} : \sup_{n\in\mathbb{Z}} \|\eta_n\| \leq M_{\mathscr{B}} \right\},$$

where $M_{\mathscr{B}}$ is a positive real number.

We say that a pair of sequences $\left(\{\eta_n^1\}, \{\eta_n^2\}\right) \in \mathscr{B}\times\mathscr{B}$ is proximal if for an arbitrary small number $\epsilon > 0$ and an arbitrary large natural number E, there exist an integer m_0 and a natural number $E_0 \geq E$ such that $\left\|\eta_n^1 - \eta_n^2\right\| < \epsilon$ for $m_0 \leq n \leq m_0 + E_0$.

It is mentioned in [3,5] that a pair of sequences $\left(\{\eta_n^1\}, \{\eta_n^2\}\right)$ is proximal if $\liminf_{n\to\infty} \left\|\eta_n^1 - \eta_n^2\right\| = 0$. It is worth saying that our definition for proximality, which is adapted to the collection $\mathscr{B}$ and needed for our extension purposes, is, in general, stronger than the one mentioned in the classical sense. Nevertheless, one can achieve the equivalence of both definitions for equations of the form (1), for example, by requesting a Lipschitz condition on the function F.

Another feature of Li-Yorke chaos is the following one. A pair of sequences $\left(\{\eta_n^1\}, \{\eta_n^2\}\right) \in \mathscr{B}\times\mathscr{B}$ is called not asymptotic if $\limsup_{n\to\infty} \left\|\eta_n^1 - \eta_n^2\right\| > 0$.

We call a pair of sequences $\left(\{\eta_n^1\}, \{\eta_n^2\}\right) \in \mathscr{B}\times\mathscr{B}$ as a Li-Yorke pair, if they are proximal and not asymptotic. On the other hand, a subset $\mathscr{C} \subset \mathscr{B}$ is called a scrambled set if it does not contain any periodic sequences and for any distinct sequences $\{\eta_n^1\}, \{\eta_n^2\} \in \mathscr{C}$, the pair $\left(\{\eta_n^1\}, \{\eta_n^2\}\right)$ is a Li-Yorke pair.

The collection $\mathscr{B}$ is called a Li−Yorke chaotic set if: (i) $\mathscr{B}$ admits a periodic sequence of period k, for any natural number k; (ii) $\mathscr{B}$ possesses an uncountable scrambled set $\mathscr{C}$; (iii) For any sequence $\{\eta_n\} \in \mathscr{C}$ and any periodic sequence $\{\xi_n\} \in \mathscr{B}$, we have $\limsup_{n\to\infty} \|\eta_n - \xi_n\| > 0$.

In the remaining parts, the uniform norm $\|\Gamma\| = \sup_{\|v\|=1} \|\Gamma v\|$ for matrices will be utilized.

The following assumptions will be needed:

(A1) There exist positive numbers L_1 and L_2 such that

$$L_1 \|x - \overline{x}\| \leq \|g(x) - g(\overline{x})\| \leq L_2 \|x - \overline{x}\|,$$

for all $x, \overline{x} \in \mathbb{R}^p$;

(A2) There exists a positive number L_3 such that

$$\|f(y) - f(\overline{y})\| \leq L_3 \|y - \overline{y}\|,$$

for all $y, \overline{y} \in \mathbb{R}^q$;

(A3) There exist positive real numbers M_f and M_g such that $\sup_{y\in\mathbb{R}^q} \|f(y)\| \leq M_f$ and $\sup_{x\in\mathbb{R}^p} \|g(x)\| \leq M_g$;

(A4) $\|A\| + L_3 < 1$.

For a given solution $x = \{x_n\}$ of equation (1), using the standard technique for maps [20], one can verify that there exists a unique bounded solution $\{\phi_n^x\}$ of equation (2). In the notation $\{\phi_n^x\}$, the symbol "x" is devoted to indicate the dependence of the bounded solution on the chosen solution $x = \{x_n\}$ of equation (1). Moreover, the unique bounded solution $\{\phi_n^x\}$, satisfies the relation

$$\phi_n^x = \sum_{j=-\infty}^{n} A^{n-j}[f(\phi_{j-1}^x) + g(x_{j-1})],\ n \in \mathbb{Z}. \tag{3}$$

Let us denote by $\mathscr{A}_x$ the set of all uniformly bounded solutions of equation (1) with initial data from the set Λ. Set $\mathscr{A}_y = \{\{\phi_n^x\} : x = \{x_n\} \in \mathscr{A}_x\}$. Equation (3) implies that for any $\{y_n\} \in \mathscr{A}_y$ the inequality $\sup_{n\in\mathbb{Z}} \|y_n\| \leq H$ holds, where $H = \dfrac{M_f + M_g}{1 - \|A\|}$.

We say that $\mathscr{A}_y$ is an attractor if for each solution $\{y_n\}$ of equation (2), there exists a solution $\{\widetilde{y}_n\} \in \mathscr{A}_y$ such that $\|y_n - \widetilde{y}_n\| \to 0$ as $n \to \infty$. We will verify the attractiveness of the set $\mathscr{A}_y$ in the next assertion.

Lemma 1. *$\mathscr{A}_y$ is an attractor.*

Proof. Consider an arbitrary solution $\{y_n\}$ of equation (2) with a fixed solution $\{x_n\}$ of equation (1). The relations

$$y_n = A^n y_0 + \sum_{j=1}^{n} A^{n-j}[f(y_{j-1}) + g(x_{j-1})],$$

$$\phi_n^x = A^n \phi_0^x + \sum_{j=1}^{n} A^{n-j}[f(\phi_{j-1}^x) + g(x_{j-1})],$$

imply for each $n \geq 1$ the inequality

$$\|A\|^{-n} \|y_n - \phi_n^x\| \leq \|y_0 - \phi_0^x\| + \frac{L_3}{\|A\|} \sum_{j=0}^{n-1} \|A\|^{-j} \left\|y_j - \phi_j^x\right\|.$$

Applying Gronwall inequality, one can obtain that

$$\|y_n - \phi_n^x\| \leq \|y_0 - \phi_0^x\| (\|A\| + L_3)^n.$$

According to condition $(A4)$, we have $\|y_n - \phi_n^x\| \to 0$ as $n \to \infty$. □

One can verify using Lemma 1 that any two solutions $\{y_n\}, \{\overline{y}_n\}$ of equation (2) with the same $\{x_n\}$ satisfy the criterion (A). Therefore, generalized synchronization occurs in equation (1)+(2).

Extension of chaos in the sense of Li-Yorke will be handled in the next section.

3 Extension of Li-Yorke chaos

In Lemma 2 and Lemma 3, we will consider the replication of the ingredients of Li-Yorke chaos, and the main result will be presented in Theorem 1.

Lemma 2. *If a pair of sequences* $(\{x_n\},\{\overline{x}_n\}) \in \mathscr{A}_x \times \mathscr{A}_x$ *is proximal, then the pair* $\left(\{\phi_n^x\},\{\phi_n^{\overline{x}}\}\right) \in \mathscr{A}_y \times \mathscr{A}_y$ *is also proximal.*

Proof. Fix an arbitrary small positive number ϵ and an arbitrary large natural number E. Let $\gamma = 1/\left(\frac{L_2}{1-\|A\|-L_3} + \frac{2(M_f+M_g)}{1-\|A\|}\right)$.

According to our assumption that the pair $(\{x_n\},\{\overline{x}_n\}) \in \mathscr{A}_x \times \mathscr{A}_x$ is proximal, there exist an integer m_0 and a natural number $E_0 \geq E$ such that $\|x_n - \overline{x}_n\| < \gamma\epsilon$ for $m_0 \leq n \leq m_0 + E_0$. Throughout the proof, let us denote $y_n = \phi_n^x$ and $\overline{y}_n = \phi_n^{\overline{x}}$, $n \in \mathbb{Z}$.

Making use of the equations

$$y_n = \sum_{j=-\infty}^{n} A^{n-j}\left[f(y_{j-1}) + g(x_{j-1})\right]$$

and

$$\overline{y}_n = \sum_{j=-\infty}^{n} A^{n-j}\left[f(\overline{y}_{j-1}) + g(\overline{x}_{j-1})\right],$$

we obtain for $n \geq m_0 + 1$ that

$$\begin{aligned} y_n - \overline{y}_n &= \sum_{j=-\infty}^{m_0} A^{n-j}\left[f(y_{j-1}) + g(x_{j-1}) - f(\overline{y}_{j-1}) - g(\overline{x}_{j-1})\right] \\ &+ \sum_{j=m_0+1}^{n} A^{n-j}\left[f(y_{j-1}) - f(\overline{y}_{j-1})\right] + \sum_{j=m_0+1}^{n} A^{n-j}\left[g(x_{j-1}) - g(\overline{x}_{j-1})\right]. \end{aligned}$$

Therefore, the inequality

$$\begin{aligned} \|y_n - \overline{y}_n\| &\leq \sum_{j=-\infty}^{m_0} 2(M_f + M_g)\|A\|^{n-j} + \sum_{j=m_0+1}^{n} L_2\gamma\epsilon\|A\|^{n-j} \\ &+ \sum_{j=m_0+1}^{n} L_3\|A\|^{n-j}\left\|y_{j-1} - \overline{y}_{j-1}\right\| \\ &= \frac{2(M_f + M_g)}{1-\|A\|}\|A\|^{n-m_0} + \frac{L_2\gamma\epsilon}{1-\|A\|}\left(1 - \|A\|^{n-m_0}\right) \\ &+ \sum_{j=m_0}^{n-1} L_3\|A\|^{n+1-j}\left\|y_j - \overline{y}_j\right\| \end{aligned}$$

holds for $m_0 + 1 \leq n \leq m_0 + E_0 + 1$. Multiplication of the both sides of the last inequality by the term $\|A\|^{-n}$ gives us

$$\|A\|^{-n}\|y_n - \overline{y}_n\| \leq \left(\frac{2(M_f + M_g) - L_2\gamma\epsilon}{1-\|A\|}\right)\|A\|^{-m_0} + \frac{L_2\gamma\epsilon}{1-\|A\|}\|A\|^{-n}$$

$$+\sum_{j=m_0}^{n-1}\frac{L_3}{\|A\|}\|A\|^{-j}\left\|y_j-\overline{y}_j\right\|.$$

By the help of the Gronwall inequality, one can attain that

$$\|A\|^{-n}\|y_n-\overline{y}_n\|\leq\left(\frac{2(M_f+M_g)-L_2\gamma\epsilon}{1-\|A\|}\right)\|A\|^{-m_0}+\frac{L_2\gamma\epsilon}{1-\|A\|}\|A\|^{-n}$$
$$+\sum_{j=m_0}^{n-1}\frac{L_3}{\|A\|}\Big[\left(\frac{2(M_f+M_g)-L_2\gamma\epsilon}{1-\|A\|}\right)\|A\|^{-m_0}$$
$$+\frac{L_2\gamma\epsilon}{1-\|A\|}\|A\|^{-j}\Big]\left(1+\frac{L_3}{\|A\|}\right)^{n-1-j}$$
$$=\frac{L_2\gamma\epsilon}{1-\|A\|}\|A\|^{-n}+\left(\frac{2(M_f+M_g)-L_2\gamma\epsilon}{1-\|A\|}\right)\|A\|^{-m_0}\left(\frac{\|A\|}{\|A\|+L_3}\right)^{m_0-n}$$
$$+\frac{L_2L_3\gamma\epsilon}{(1-\|A\|)(1-\|A\|-L_3)}\|A\|^{-n}\left(1-(\|A\|+L_3)^{n-m_0}\right).$$

Thus, we have

$$\|y_n-\overline{y}_n\|\leq\frac{L_2\gamma\epsilon}{1-\|A\|}+\left(\frac{2(M_f+M_g)-L_2\gamma\epsilon}{1-\|A\|}\right)(\|A\|+L_3)^{n-m_0}$$
$$+\frac{L_2L_3\gamma\epsilon}{(1-\|A\|)(1-\|A\|-L_3)}\left(1-(\|A\|+L_3)^{n-m_0}\right)$$
$$=\frac{2(M_f+M_g)}{1-\|A\|}(\|A\|+L_3)^{n-m_0}+\frac{L_2\gamma\epsilon}{1-\|A\|-L_3}\left(1-(\|A\|+L_3)^{n-m_0}\right)$$
$$\leq\frac{2(M_f+M_g)}{1-\|A\|}(\|A\|+L_3)^{n-m_0}+\frac{L_2\gamma\epsilon}{1-\|A\|-L_3}.$$

Suppose that the natural number E is sufficiently large such that

$$\left\lfloor\frac{E}{2}\right\rfloor>\frac{\ln(\gamma\epsilon)}{\ln(\|A\|+L_3)}-1,$$

where $\left\lfloor\frac{E}{2}\right\rfloor$ denotes the greatest integer which is not larger than $E/2$.

Under the circumstances, if $m_0+\left\lfloor\frac{E}{2}\right\rfloor+1\leq n\leq m_0+E_0+1$, then

$$(\|A\|+L_3)^{n-m_0}<\gamma\epsilon,$$

and hence the inequality

$$\|y_n-\overline{y}_n\|<\left(\frac{L_2}{1-\|A\|-L_3}+\frac{2(M_f+M_g)}{1-\|A\|}\right)\gamma\epsilon=\epsilon$$

is obtained. As a consequence, the pair $\left(\{\phi_n^x\},\{\phi_n^{\overline{x}}\}\right)\in\mathscr{A}_y\times\mathscr{A}_y$ is proximal. □

Lemma 3. *If a pair of sequences* $(\{x_n\},\{\overline{x}_n\})\in\mathscr{A}_x\times\mathscr{A}_x$ *is not asymptotic, then the same is true for the pair* $\left(\{\phi_n^x\},\{\phi_n^{\overline{x}}\}\right)\in\mathscr{A}_y\times\mathscr{A}_y$.

Proof. By means of equation (2) one can show for a pair $(\{x_n\},\{\overline{x}_n\}) \in \mathscr{A}_x \times \mathscr{A}_x$ that

$$\left\|\phi^x_{k+1} - \phi^{\overline{x}}_{k+1}\right\| \geq \|x_k - \overline{x}_k\| - (\|A\| + L_3)\left\|\phi^x_k - \phi^{\overline{x}}_k\right\|,\ k \in \mathbb{Z}.$$

Therefore, we have

$$\sup_{k\geq n}\left\|\phi^x_{k+1} - \phi^{\overline{x}}_{k+1}\right\| \geq \sup_{k\geq n}\|x_n - \overline{x}_k\| - (\|A\| + L_3)\sup_{k\geq n}\left\|\phi^x_k - \phi^{\overline{x}}_k\right\|$$

for any $n \in \mathbb{Z}$. The last inequality implies that

$$\sup_{k\geq n}\left\|\phi^x_{k+1} - \phi^{\overline{x}}_{k+1}\right\| \geq \frac{1}{1+\|A\|+L_3}\sup_{k\geq n}\|x_k - \overline{x}_k\|. \tag{4}$$

Since $(\{x_n\},\{\overline{x}_n\}) \in \mathscr{A}_x \times \mathscr{A}_x$ is assumed to be not asymptotic, we have that

$$\limsup_{n\to\infty}\|x_n - \overline{x}_n\| = \lim_{n\to\infty}\left(\sup_{k\geq n}\|x_k - \overline{x}_k\|\right) > 0.$$

Thus, making use of inequality (4), one can verify that

$$\limsup_{n\to\infty}\left\|\phi^x_{n+1} - \phi^{\overline{x}}_{n+1}\right\| = \lim_{n\to\infty}\left(\sup_{k\geq n}\left\|\phi^x_k - \phi^{\overline{x}}_k\right\|\right) > 0.$$

Consequently, the pair $\left(\{\phi^x_n\},\{\phi^{\overline{x}}_n\}\right) \in \mathscr{A}_y \times \mathscr{A}_y$ is not asymptotic. □

The main theorem of the present paper is the following one.

Theorem 1. *If $\mathscr{A}_x$ is a Li-Yorke chaotic set, then the same is true for $\mathscr{A}_y$.*

Proof. Assume that the set $\mathscr{A}_x$ is Li-Yorke chaotic. One can show that for any natural number k, the sequence $x = \{x_n\} \in \mathscr{P}_x$ is $k-$periodic if and only if $\{\phi^x_n\}$ is $k-$periodic. Therefore, the set $\mathscr{A}_y$ admits a $k-$periodic sequence for any natural number k. Denote by $\mathscr{P}_x$ the set of periodic solutions of (1), and let

$$\mathscr{P}_y = \{\{\phi^x_n\} :\ x = \{x_n\} \in \mathscr{P}_x\}.$$

Suppose that the set $\mathscr{C}_x$ is an uncountable scrambled set inside $\mathscr{A}_x$. Define the set $\mathscr{C}_y = \{\{\phi^x_n\} :\ x = \{x_n\} \in \mathscr{C}_x\}$. Condition $(A1)$ implies that there is a one-to-one correspondence between the elements of $\mathscr{C}_x$ and $\mathscr{C}_y$. Therefore, $\mathscr{C}_y$ is uncountable. Moreover, using the same condition one can show that no periodic sequences exist inside $\mathscr{C}_y$, since no such sequences take place inside $\mathscr{C}_x$.

Since the collection $\mathscr{A}_x$ is assumed to be chaotic in the sense of Li-Yorke, each pair of sequences inside $\mathscr{C}_x \times \mathscr{C}_x$ is proximal. Lemma 2 implies that the same feature is valid for each pair inside $\mathscr{C}_y \times \mathscr{C}_y$. On the other hand, according to Lemma 3, any couple $(\{y_n\},\{\overline{y}_n\}) \in \mathscr{C}_y \times \mathscr{C}_y$ satisfies the property that $\limsup_{n\to\infty}\|y_n - \overline{y}_n\| > 0$. Hence, the set $\mathscr{C}_y$ is an uncountable scrambled set inside $\mathscr{A}_y$. Moreover, each pair inside $\mathscr{C}_y \times \mathscr{P}_y$ is also not asymptotic, since the same is true for each pair inside $\mathscr{C}_x \times \mathscr{P}_x$. Consequently, $\mathscr{A}_y$ is Li-Yorke chaotic. □

4 An example

In this part, as the source of chaotic perturbations, we will use the logistic map

$$x_{n+1} = \mu x_n(1 - x_n), \tag{5}$$

where μ is a parameter and $x_0 \in \Lambda = [0, 1]$. If $0 < \mu \leq 4$ then the set Λ is invariant under the iterations of equation (5) [14]. For the parameter value $\mu = 3.9$, Li-Yorke chaos takes place in the dynamics of the logistic map [1].

Let us consider the map

$$\begin{aligned} y_{n+1} &= -\frac{1}{4}y_n + \frac{1}{6}z_n + \frac{1}{3}y_n^3, \\ z_{n+1} &= \frac{1}{5}y_n + \frac{1}{10}z_n. \end{aligned} \tag{6}$$

Equation (6) possesses a stable equilibrium point, and does not admit chaos.

We perturb equation (6) by the solutions of (5) with the parameter value $\mu = 3.9$, and set up the equation

$$\begin{aligned} y_{n+1} &= -\frac{1}{4}y_n + \frac{1}{6}z_n + \frac{1}{3}y_n^3 + \tan\left(\frac{x_n}{4}\right), \\ z_{n+1} &= \frac{1}{5}y_n + \frac{1}{10}z_n + \frac{1}{2}e^{x_n}. \end{aligned} \tag{7}$$

Equation (7) is in the form of (2), where $A = \begin{pmatrix} -1/4 & 1/6 \\ 1/5 & 1/10 \end{pmatrix}$. The conditions $(A1), (A2)$ are satisfied with $L_1 = 3\sqrt{2}/8$, $L_2 = (e + 1)/2$ and $L_3 = 0.16$. One can verify that condition $(A4)$ holds for equation (7).

In compliance with Theorem 1, the chaos of the logistic map (5) is extended through equation (7). Moreover, the dynamics of equation (5)+(7) exhibits generalized synchronization.

Let us consider a solution of equation (5)+(7) with $x_0 = 0.46$, $y_0 = 0.35$ and $z_0 = 1.23$. Figure 1 depicts the y and z coordinates of the solution. Figure 1 supports our theoretical results such that the solution behaves chaotically.

5 Discussions

In this part of the paper, we will discuss through simulations the extension of chaos around closed invariant curves of discrete maps and replication of intermittency.

5.1 Chaos extension around closed invariant curves

Consider the delayed logistic map [14,25], which is represented by the equation

$$\begin{aligned} y_{n+1} &= z_n, \\ z_{n+1} &= \lambda z_n(1 - y_n), \end{aligned} \tag{8}$$

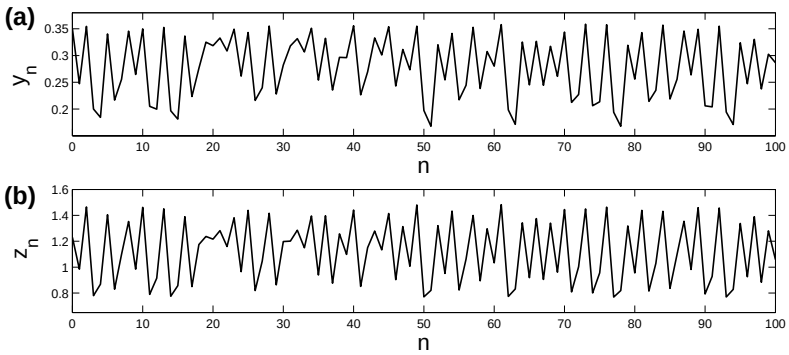

Fig. 1. The extension of chaos in equation (7). (a) The graph of y-coordinate; (b) The graph of z-coordinate. The parameter value $\mu = 3.9$ is used in the map (5) such that Li-Yorke chaos takes place. The presented pictures support the theoretical results such that the chaos of the logistic map is extended.

where λ is a positive real parameter.

Equation (8) describes a population dynamics model, where z_n is the density of a population at time n, and λ is the growth rate. In this model, the growth is determined not only by the current population but also by its density in the past [25].

According to the results mentioned in [14,25], for the parameter value $\lambda = \lambda_0 \equiv 2$, the fixed point $(1/2, 1/2)$ of equation (8) undergoes a supercritical Neimark-Sacker bifurcation. In other words, for $\lambda > 2$ and $\lambda - 2$ sufficiently small, the delayed logistic map has a unique attracting closed invariant curve encircling the fixed point $(1 - 1/\lambda, 1 - 1/\lambda)$.

We use the value $\lambda = 2.01$ from the book [14], and perturb equation (8) by the solutions of the logistic map (5) with the parameter value $\mu = 3.9$ to set up the equation

$$\begin{aligned} y_{n+1} &= z_n + 0.0045x_n, \\ z_{n+1} &= 2.01z_n(1 - y_n). \end{aligned} \tag{9}$$

Let us consider the trajectory of equation (5)+(9) with $x_0 = 0.4209$, $y_0 = 0.4316$ and $z_0 = 0.4717$. Figure 2 depicts the projection of this trajectory for $0 \leq n \leq 10000$ on the $y - z$ plane. One can see in the figure that the solution behaves chaotically around the stable invariant curve of equation (8). This picture reveals that our theoretical results can be used not only for systems with stable equilibrium points but also with attracting closed curves.

5.2 Replication of intermittency

We will discuss the extension of intermittency [26] in this subsection through simulations.

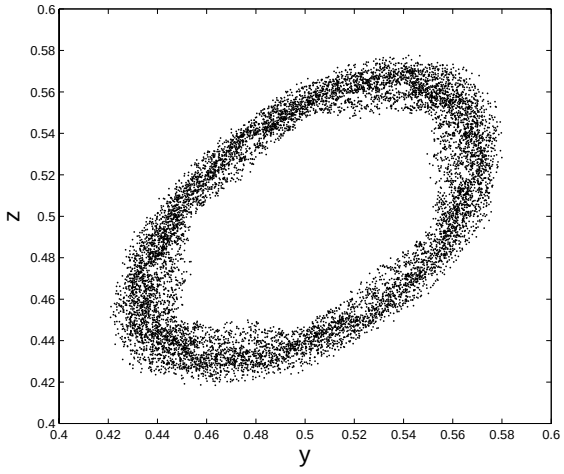

Fig. 2. Chaotic behavior in the perturbed delayed logistic equation (9).

The logistic map (5) with the parameter value $\mu = 3.828$ is known to exhibit chaos through intermittency [27]. We perturb the equation

$$y_{n+1} = \frac{1}{2}y_n + 0.002y_n^3, \tag{10}$$

by solutions of the logistic map (5) with the parameter value $\mu = 3.828$, and constitute the equation

$$y_{n+1} = \frac{1}{2}y_n + 0.002y_n^3 + 3x_n. \tag{11}$$

One can verify that the conditions $(A1) - (A4)$ are valid for equation (11).

To illustrate the replication of intermittency, in Figure 3, we visualize the graphs of both coordinates of the solution of equation (5) + (11) with $x_0 = 0.1608$, $y_0 = 4.3641$. Figure 12 reveals the extension of intermittency such that the pictures in (a) and (b) indicate the interruption of regular motions by sporadic bursts of chaotic behavior, in the logistic map and equation (11), respectively. It is also seen that equation (11) mimics the regular/irregular behavior of the logistic map with a delay, which is a expectable behavior due to the construction of the equation (1) + (2).

6 Conclusion

In the present paper, we provide a theoretical method for replication of chaos in discrete-time dynamics in such a way that the ingredients of chaos from a prior discrete equation are mimicked by a secondary one. We make use of the ingredients of chaos in the sense of Li-Yorke and investigate numerically the replication of intermittency. Chaos extension around closed invariant curves

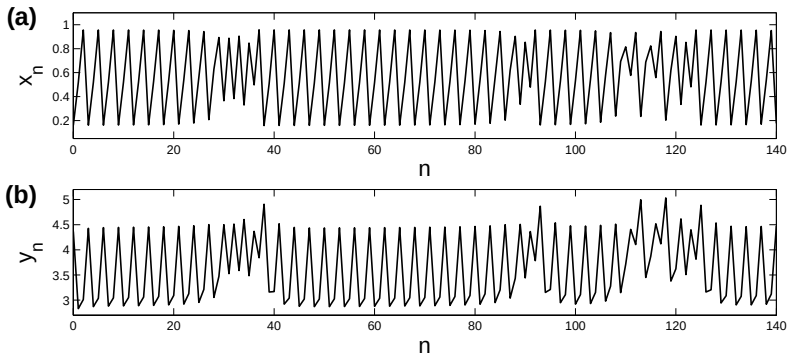

Fig. 3. Extension of intermittency in equation (11). The picture in (a) represents the intermittent behavior in the logistic map, while the picture in (b) indicate its replication in equation (11). It is observable in the figure that the $y-$coordinate mimics the regular/irregular behavior of the $x-$coordinate with a delay.

is also discussed through an example. It is worth noting that the extension procedure is valid without any constraints on the dimensions of the considered equations. As a result, a chaotic attractor in a high dimensional phase space takes place.

In the classical input/output problems, generally, one considers single functions as the input and the output. However, in the solution of the chaos extension problem, we have taken into account the concept of collection of sequences, since there is no definition for a solely chaotic sequence in discrete-time as well as in continuous-time dynamics. From the input/output problem point of view, our results emphasize that both the input and the output are chaos of the same type for the discussed equation.

Acknowledgments
This research was supported by the Grant 111T320 from TUBITAK, the Scientific and Technological Research Council of Turkey.

References

1.T.Y. Li and J.A. Yorke. Period three implies chaos. The American Mathematical Monthly, 82:985-992, 1975.
2.F.R. Marotto. Snap-back repellers imply chaos in $\mathbb{R}^n$. J. Math. Anal. Appl., 63:199-223, 1978.
3.M. Ciklová. Li-Yorke sensitive minimal maps. Nonlinearity, 19:517-529, 2006.
4.P. Kloeden and Z. Li. Li-Yorke chaos in higher dimensions: a review. J. Diff. Equ. Appl., 12:247-269, 2006.
5.E. Akin and S. Kolyada. Li-Yorke sensitivity. Nonlinearity, 16:1421-1433, 2003.
6.R.L. Devaney. An Introduction to Chaotic Dynamical Systems. Addison-Wesley, United States of America, 1987.
7.S. Smale. Differentiable dynamical systems. Bull. Amer. Math. Soc. 73:747-817, 1967.

8.J. Kennedy and J.A. Yorke. Topological horseshoes. Transactions of the American Mathematical Society 353:2513-2530, 2001.
9.A.C.J. Luo. Regularity and Complexity in Dynamical Systems. Springer, New York, 2012.
10.S. Wiggins. Global Bifurcations and Chaos: Analytical Methods. Springer-Verlag, New York, 1988.
11.R. Brown. Horseshoes in the measure preserving Hénon map. Ergod. Th. Dynam. Syst. 15:1045-1059, 1995.
12.R. Devaney and Z. Nitecki. Shift automorphism in the Hénon mapping. Comm. Math. Phys. 67:137-148, 1979.
13.J. Guckenheimer and P. Holmes. Nonlinear Oscillations, Dynamical Systems, and Bifurcations of Vector Fields. Springer-Verlag, New York, 1997.
14.J. Hale and H. Koçak. Dynamics and Bifurcations. Springer-Verlag, New York, 1991.
15.E.N. Lorenz. Deterministic nonperiodic flow. J. Atmos. Sci 20:130-141, 1963.
16.M. Cartwright and J. Littlewood. On nonlinear differential equations of the second order I: The equation $\ddot{y} - k(1 - y^2)'y + y = bk\cos(\lambda t + a)$, k large. J. London Math. Soc. 20:180-189, 1945.
17.N. Levinson. A second order differential equation with singular solutions. Ann. of Math. 50:127-153, 1949.
18.M. Levi. Qualitative Analysis of the Periodically Forced Relaxation Oscillations. Memoirs of the American Mathematical Society, United States of America, 1981.
19.C. Corduneanu. Almost Periodic Oscillations and Waves. Springer, New York, 2009.
20.V. Lakshmikantham and D. Trigiante. Theory of Difference Equations: Numerical Methods and Applications. Marcel Dekker, United States of America, 2002.
21.N.F. Rulkov, M.M. Sushchik, L.S. Tsimring and H.D.I. Abarbanel. Generalized synchronization of chaos in directionally coupled chaotic systems. Phys. Rev. E, 51:980-994, 1995.
22.L. Kocarev and U. Parlitz. Generalized synchronization, predictability, and equivalence of unidirectionally coupled dynamical systems. Phys. Rev. Lett., 76:1816-1819, 1996.
23.V. Afraimovich, J.-R. Chazottes and A. Cordonet. Nonsmooth functions in generalized synchronization of chaos. Physics Letters A, 283:109-112, 2001.
24.A.A. Koronovskii, O.I. Moskalenko, S.A. Shurygina and A.E. Hramov. Generalized synchronization in discrete maps. New point of view on weak and strong synchronization. Chaos, Solitons & Fractals 46:1218, 2013.
25.Y.A. Kuznetsov. Elemets of Applied Bifurcation Theory. Springer, New York, 1998.
26.Y. Pomeau and P. Manneville. Intermittent transition to turbulence in dissipative dynamical systems. Commun. Math. Phys. 74:189-197, 1980.
27.S.N. Elaydi. Discrete Chaos: With Applications in Science and Engineering. Chapman & Hall/CRC, 2008.

Chaotic Modeling and Simulation (CMSIM) 2: 141-152, 2014

Geometry of chaos – the Bernoulli equation for ternary and quaternary alloys

E. M. Sheregii
University of Rzeszow, Center of Microelectronics and Nanotechnology, Rzeszow, Poland
E-mail: sheregii@univ.rzeszow.pl

Abstract: To understand and interpret the experimental data on the phonon spectra of the solid solutions it is necessary to describe mathematically the non-regular distribution of atoms in its lattices. It occurs that such description is possible in case of the strongly chaotically (stochastically) homogenous distribution what require a very great number of atoms and a very carefully mixed alloys. These conditions are fulfilled generally in case of the high quality homogenous semiconductor solid solutions of the III-V and II-VI semiconductor compounds. In this case we can use the Bernoulli equation describing a probability to occur a one from *n* equivalent events what can be apply to the probability to find one from *n* configurations in the solid solution lattice. The results described in this paper for ternary HgCdTe and quaternary HgZnCdTe can give affirmative answer on the question: whether geometry of chaos e.g. the Bernoulli equation is enough to describe the observed phonon spectra.
Keywords: Chaotic modeling, Phonon spectra, Solid solutions, Chaotic simulation.

1. Introduction

The role of alloys of semiconductors in electronics and optoelectronics is constantly increasing; more and more devices (lasers, convertors, detectors, memory elements etc.) are based on semiconductor solid solutions – another name for alloys. A homogenous high quality solid solution with the substitution of a cation or anion (we consider here mainly the semiconductor compounds III-V and II-VI) should be characterized by the random distribution of atoms in a lattice. However, we cannot call this a crystalline lattice because it does not possess one very important feature of crystals – long-acted ordering. From the point of view of electronic structuring it means some fluctuations of periodic potential exist in relation to different atoms (cation or anion) in the structurally reproducible basic cell in the lattice – a tetrahedron in the case of a zinc-blend structure and wurzit structure. Experiments have shown that electrons having a long-length wave function (belonging to the minimum in the center of the Brilluoin zone) are practically insensitive to these fluctuations and a *k*-vector can be attributed to electrons as a "good" quantum number.

A different situation occurs, in principal, in the case of the phonon spectra in mixed crystals. The atom masses (cation or anion) in a structurally reproducible cell are not repeated for different cells in the lattice because of the chaotic (random) distribution of the "foreign" atoms. This means that

Received: 7 August 2013 / Accepted: 12 April 2014
© 2014 CMSIM
ISSN 2241-0503

definitively different vibration frequencies of the dipole pairs presented in cells exist in the case of optical oscillations. Thus, the phonon spectrum of alloys behaves ambivalently: usually the optical phonon branches split into several modes proper to the mass of the components of the mixed crystal lattice; although research contributions about one-mode behavior exist also [1]. The principally important question is: whether these vibrations of different dipole pairs are connected in the alloy lattice and form a running wave (phonons) with dispersion relations or, to the contrary: they are disseminated on a great number of local modes? This question is connected with another problem concerning the local structure of solid solutions: that which can be described by the random distribution of atoms – the geometry of chaos – or is this geometrical factor not sufficient and it is necessary to add a thermodynamic factor?

In this paper we attempt to generalise the experimental results obtained from the ternary $Hg_{1-x}Cd_xTe$ and quaternary $Zn_yCd_xHg_{1-x-y}Te$ far-infrared spectra (FIR-spectra) using synchrotron radiation as source in the far-infrared region. Their interpretation based on the Bernoulli equation can, in part, respond to the formulated above questions concerning the phonon spectra of these materials.

2. The Model

To understand and interpret the experimental data on the phonon spectra of the solid solutions it is necessary to describe mathematically the non-regular distribution of atoms in its lattices. It occurs that such description is possible in case of the strongly chaotically (stochastically) homogenous distribution what require a very great number of atoms and a very carefully mixed alloys. These conditions are fulfilled generally in case of the high quality homogenous semiconductor solid solutions of the III-V and II-VI semiconductor compounds. In this case we can use the Bernoulli equation [2] describing a probability to occur a one from n equivalent events what can be apply to the probability to find one from n configurations in the solid solution lattice.

The crystalline structure of the most III-V and II-VI compounds (possessed zinc-blend or wurzit structure as was mentioned above) is characterized by basic cell – tetrahedron – each with a central ion surrounded in the first coordination shell by four nearest neighbours (NN) at the vertices. In a $A_{1-x}B_xZ$ ternary solid solution with substitution of the cation A by cation B, different tetrahedron configurations Tn (n is the number of B-atoms in the tetrahedron) coexist simultaneously: 2 strictly-binary ones corresponding to the AZ and the BZ compounds, whose lattices are characterized by the tedrahedron units T0 and T4 (configurations), respectively and 3 strictly-ternary ones actually characterized by the configurations T1, T2 and T3. The similar configurations exist in a AY_yZ_{1-y} solid solution where anions Z are substituted by anions Y – the tetrahedra will be looked at similarly because in zinc-blend lattice we can represent a basic unit as tetrahedron in two versions: centred by anion and surrounded by four cations or oppositely: four anions surrounded cation in centre.

The probability to find the Tn configuration in ideal lattice of the $A_{1-x}B_xZ$ or AY_yZ_{1-y} ternary solid solution can be find using the Bernoulli polynomial [2]:

$$P_n(x)=\binom{4}{n}(1-x)^{4-n}x^n \tag{1}$$

where $\binom{4}{n}=\frac{4!}{n!(4-n)!}$ is the number of combinations with n elements in the fourth set:

$$\binom{4}{0}=\binom{4}{4}=1,\binom{4}{1}=\binom{4}{3}=4,\binom{4}{2}=6,$$

x is a mol composition of BZ compound in the solid solution what is equal to the ratio of the B-Z ion pairs per whole number of ion pairs in lattice.

It is obvious that probability $P_n(x)$ must be function of composition x because increasing of x means increasing of the B-atoms number in lattice what leads to increasing of the tetrahedron's number with high value of n (not higher then 4). The sum of probabilities to find all configurations in lattice of alloy with composition x must be equal to 1:

$$\sum_n^4 P_n(x)=1 \tag{2}$$

The probabilities to find a some of cation A or B respectively are:

$$P_n^A(x)=\frac{4-n}{4}\binom{4}{n}(1-x)^{4-n}x^n \tag{3}$$

$$P_n^B(x)=\frac{n}{4}\binom{4}{n}(1-x)^{4-n}x^n \tag{4}$$

It is easy to determine that

$$\sum_n^4 P_n^A(x)=1-x \tag{5}$$

$$\sum_n^4 P_n^B(x)=x \tag{6}$$

It is necessary to note that (3) and (4) are simultaneously the probabilities to find in the solid solution lattice the ion pairs A-Z and B-Z.

The oscillator strength of the vibrational mode generated by a *A*-*Z*-dipole in the T_n configuration is [3]:

$$S_n^{A-Z}(x)=f_{AZ}N_0P_n^A(x) \tag{7}$$

where f_{AZ} is the oscillator strength of the single dipole *A*-*Z*-pair, N_0 is number of dipole pairs A-Z in the solid solution crystal, probability $P_n^A(x)$ is determined by (3).

It is important to remember that three assumption are introduced in this consideration:

1) the role of defects is negligible;
2) the alloy lattice is ideally homogenous and a random distribution of atoms in lattice takes place (stochastic homogeneity);
3) the oscillator strengths of the single dipole pairs for different configurations T_n are the same e.g. f_{AZ} or f_{BZ} depends not on index n.

If these conditions are fulfilled, the oscillator sum rule

$$\sum_n S_n^{A-Z}(x) = \sum_n f_{AZ} N_0 P_n^A(x) = f_{AZ} N_0 \sum_n P_n^A(x) = f_{AZ} N_0 (1-x) \qquad (8)$$

has to be satisfied.

Similarly for *B-Z* dipole pairs:

$$S_n^{B-Z}(x) = f_{BZ} N_0 P_n^B(x) \qquad (9)$$

and oscillator sum rule

$$\sum_n S_n^{B-Z}(x) = \sum_n f_{BZ} N_0 P_n^B(x) = f_{AZ} N_0 \sum_n P_n^B(x) = f_{BZ} N_0 x \qquad (10)$$

The experimental Im ε(ω)-curves (obtained by Kramers-Kroning transformation from experimentally measured *R(ω)*-curve [4]) enable us to find the S_i values, to identify that with certain S_n^{A-Z} or S_n^{B-Z} and to verify the sums (9) or (10) what means the proportionality of the oscillator sum to the contain of the each component in alloy (N_0x is equal to molar percent of the *BZ* component and $N_0(1-x)$ – to the molar percent of the component *AZ*).

We consider here also the four-component solid solution $A_xB_y\ C_{1-x-y}Z$ with three kinds of cations *A, B* and *C* and with the same anion *Z*. The lattice of quaternary alloy contents 15 basic units (tetrahedra): three binary *AZ, BZ, CZ* and nine strictly ternary *ABZ, ACZ, BCZ* . If quaternary alloy have *x* mol part of *AZ* compound and *y* mol part of *BZ* we can determine the probability to find in lattice the tetrahedron T_{nm} with *n* A-cations and *m* B-cations. This probability is equal to:

$$P_{n,m}(x,y) = \binom{4-n}{m}\binom{4}{n}(1-x-y)^{4-n-m} x^n y^m \qquad (11)$$

where matrixes $\binom{4-n}{m}$ and $\binom{4}{n}$ are the same number of combinations as in Eqn. (1).

The correspond probabilities to find particular cations in lattice are:

$$P_n^A(x) = \frac{n}{4}\binom{4-n}{m}\binom{4}{n} x^n y^m (1-x)^{4-n-m}, \qquad (12)$$

for cation *A*;

$$P_n^B(x) = \frac{m}{4}\binom{4-n}{m}\binom{4}{n} x^n y^m (1-x)^{4-n-m}, \qquad (13)$$

for cation *B*, and

$$P_n^C(x) = \frac{4-n-m}{4}\binom{4-n}{m}\binom{4}{n} x^n y^m (1-x)^{4-n-m} \qquad (14)$$

for cation *C*.

By this way the Eqns. (3,4,7,8, 10, 12 – 14) [5] represent the complete description of the random atom distribution in the ternary $A_xB_{1-x}Z$ and quaternary $A_xB_y\ C_{1-x-y}Z$ solid solutions with substitution of cations. The four-component solid solution $A_xB_yC_{1-x-y}Z$ in ideally random case described by relations (11) and (12-14) consists from fifteen structural units – tetrahedra – which can generate 66 optically active phonon (vibrational) modes. These number of modes arose by next way: three strictly binary tetrahedra generate three vibrational modes AZ-like, BZ-like and CZ-like, nine (3x3) strictly ternary tetrahedra generate 9x6=54 vibrational modes and three strictly quaternary tetrahedra generate 3x3=9 vibrational modes: in sum 66 vibrational modes. In practice the most of these modes are degenerated (have the same frequencies): for example, the AZ-like modes generated in tetrahedra ABZ could have the same frequencies as AZ-like modes in tetrahedra ACZ. The same concerns the BZ-like and CZ-like modes. By this way the number of distinguished modes should be 30.

The expression for the oscillator strengths are similar as for ternary alloys:

$$S_{n,m}^{A-Z}(x,y) = f_{AZ}N_0P_{n,m}^{A}(x,y) \tag{15}$$

where probability $P_{n,m}^{A}(x,y)$ is determined by (14). Similarly are given the expression for $S_{n,m}^{B-Z}$ and $S_{n,m}^{C-Z}$. The corresponding oscillator sum rule are:

$$\sum S_{n,m}^{A-Z} = N_0 f_{AZ}(1-x-y) \tag{16}$$

$$\sum S_{n,m}^{B-Z} = N_0 f_{BZ}x \tag{17}$$

$$\sum S_{n,m}^{C-Z} = N_0 f_{CZ}y \tag{18}$$

The role of these oscillator sum rules (16-18) would be the same as in ternary alloys (8,10) but in the practice it is more difficult to relies the verification of the random distribution of atoms because the number of theoretically possible modes is very large and this factor prevent calculation of the oscillator sum rule.

3. Experimental results and interpretation

Here will be presented the results on FIR-spectra for ternary and quaternary alloys in order to illustrate application of presented above model for interpretation these experimental spectra. The optical reflection spectra in the region from 10 to 10 000 cm^{-1} where the phonon frequency values (100 – 400 cm^{-1}) of semiconductor's compounds are located, were measured in the wide temperature interval and composition regions. Experiments were performed at the DAFNE-light laboratory at Frascati (Italy) using the experimental set-up described in paper [6].

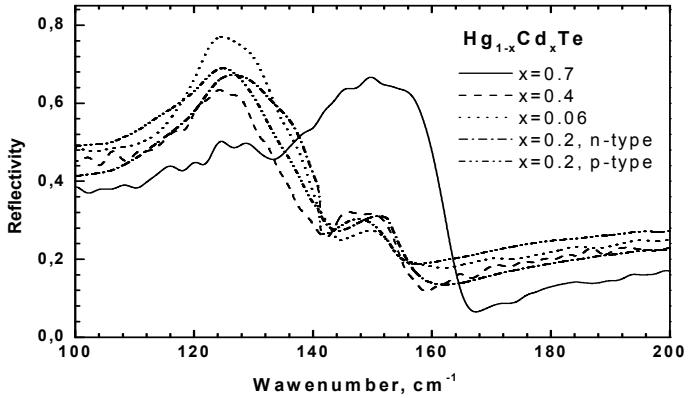

Fig.1. Reflectivity spectra for $Hg_{1-x}Cd_xTe$ (x is changing from 0.06 to 0.7) obtained at 300K .

The high-resolution reflection FIR-spectra obtained for the ternary $Hg_{1-x}Cd_xTe$ for compositions from x=0.06 to x=0.7 at a temperature 300K and in the spectral range from 100 cm^{-1} to 200 cm^{-1} are shown in Fig.1 as reflectivity curves R(ω). Two bands which shift weakly with the composition, are observed: first one around 118-128 $cm^{-1}$and second one around 145-155cm^{-1}. The amplitude of first band increases when the content of *HgTe* increases and amplitude of second band increases when the *CdTe* content increases. The first band corresponding to the *HgTe*-like sub-band and second sub-band is the *CdTe*-like one. This type of a reflectance spectrum again shows according to previous works [7,8,9] a two-mode behavior of the optical phonons in the $Hg_{1-x}Cd_xTe$ alloys from one hand. From other one, the subtle structure of both sub-bands is clearly observed too what undoubtedly indicates on multi-mode character of the phonon spectra (above two modes). Authors [10] interpreted these subtle structure in frame of the random model but they limited consideration of the FIR-spectra in the spectral region 118 – 160 cm^{-1}. Whereas, in the region 90 – 116 cm^{-1} are observed additional lines (we can call them as Additional Phonon Modes (APM) whereas the main sub-bands we can called as Canonical Phonon Modes (CPM)), registered earlier in the above mentioned References.

Optical reflectivity from surface of $Zn_xCd_yHg_{1-x-y}Te$. The measurements of reflectivity were performed in temperature region from 30 K to 300 K. In Fig. 2 are presented reflectivity FIR-spectra obtained for composition x=0.05, y=0.23 for three temperatures: 30 K, 100K and 300 K. These curves are similar to typical reflection spectra but these curves have a much richer structure of spectra, as were observed for ternary alloys. It is seen three main bands at 130 cm^{-1}, 160 cm^{-1} and 180 cm^{-1} which can be point out in the reflective spectra. However, each of these sub-bands has additional subtle

structures, which point to the superposition of a greater number of lines. With increasing of temperature from 30 K to 300 K the subtle structure of observed sub-bands becomes more smooth.

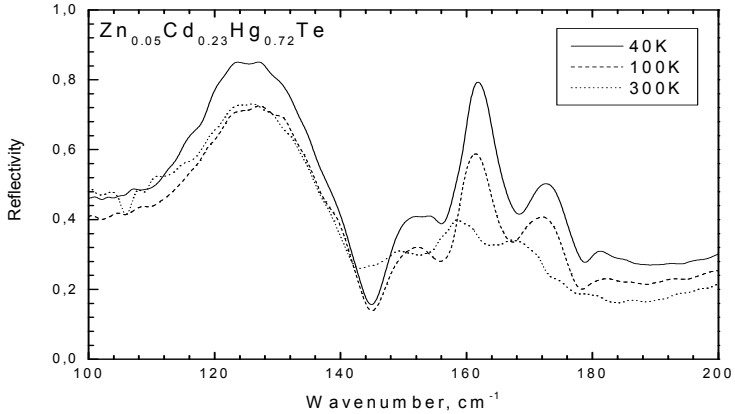

Fig.2. Reflectivity Spectra of $Zn_{0,05}Cd_{0,23}Hg_{0,72}Te$.

The lines corresponding to phonon modes are clearly observed on the *Im[ε(ω)]* curves calculated by Kramers-Kroning analyses from the experimental FIR reflectivity curves *R(ω)*.In an attempt to treat the measured reflection spectra *R(ω,y)* of semiconductor materials (such as MCT with a considerable concentration of free carriers) in a reproducible way, as well as minimizing uncertainties due to subjective manual intervention, we have strictly abided by the rough procedure described in [4]. In Fig. 3 and 4 are shown *Im[ε(ω)]*–curves for *p*-$Hg_{0.8}Cd_{0.2}Te$ obtained for temperature 300 K and for $Zn_{0,05}Cd_{0,23}Hg_{0,72}Te$, respectively. The dispersion analysis of the CPMs and APMs was performed by approximating the *Im[ε(ω,T)]* curves by the Lorentzian sum

$$\operatorname{Im}\varepsilon(\omega)=\sum_{i=1}^{k}\frac{S_i\gamma_i\omega}{(\omega_{TOi}^2-\omega^2)^2+\omega^2\gamma_i^2} \tag{22}$$

where S_i, ω_{TOi} and γ_i are the oscillator strength, frequency and damping parameter of the *i*-phonon mode, respectively.

The results of spectral analysis for *p-$Hg_{0.8}Cd_{0.2}Te$* are presented in Fig.3 and for *n-$Hg_{0.8}Cd_{0.2}Te$ in Fig.* 4. Parameters of Lorentzian's oscillators used for fitting the *Im[ε(ω,T)]*-curves are shown in Table 1.

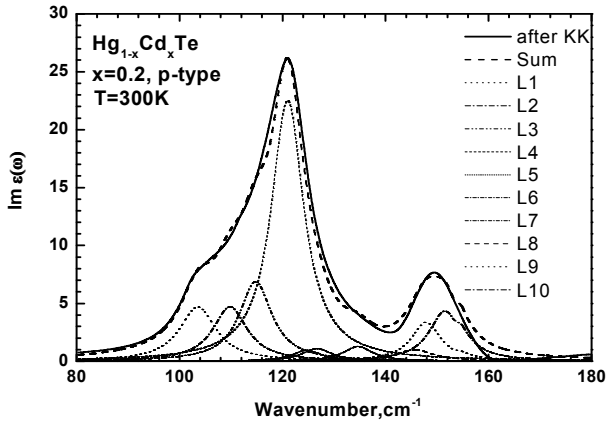

Fig.3. Imaginary part of the dielectric function od $Hg_{0,8}Cd_{0,2}Te$ *p*- type in the temperature 300K.

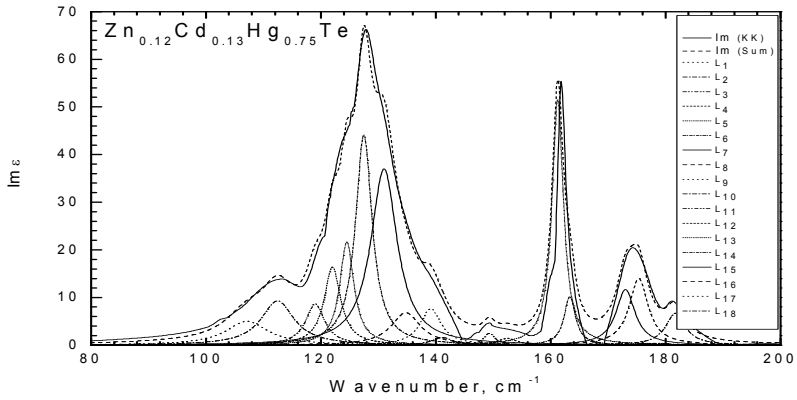

Fig. 4. Spectral analysis for sample $Zn_{0,12}Cd_{0,13}Hg_{0,75}Te$.

To identify observed lines, the probability to find the atoms Hg and Cd in the particular tetrahedra T_n (*n* is number of the Cd-atoms in tetrahedral) in the $Hg_{0.8}Cd_{0.2}Te$ lattice should be taken into account using formulas (3) and (4). If *x*=0.2 the values of $P_n^{Hg}(x)$ for different *n* are equal to: 0.410 (*n*=4), 0.307(*n*=2), 0.077(*n*=3) and 0.006(*n*=4) while the $P_n^{Cd}(x)$ values are: 0.102(*n*=1), 0.077(*n*=2), 0.192(*n*=3) and 0.002(*n*=4).

Table 1. Parameters of Lorentzian's oscillators used for fitting the *Im[ε(ω,T)]* –curves of the *p- $Hg_{0.8}Cd_{0.2}Te$* for the temperature 300K.

Number of Line	S	ω	γ	$\sum S_{HgTe}$		$\sum S_{CdTe}$	
				CPM	AVM	CPM	AVM
1	4200	103.7	8.6				
2	4200	110.0	8.1		11400		
3	6100	115.0	7.7				
4	21100	121.3	7.7				
5	830	125.0	7.0	31300			
6	1000	127.0	7.0				
8	1200	135.0	7.0				1000
9	1300	146.1	8.9			9690	
10	3500	148.3	7.0				
11	4890	152.0	7.4				

At T=30 K all HgTe-like CPMs oscillate at the same frequency because tetrahedra with different number *n* are not deformed and we observed a degeneration of vibrational modes (Hg-Te and Cd-Te bonds have the same length). If T=300 K the splitting of the mode frequency takes place: the most strong line at 122.6 cm^{-1} should be generate by Hg-Te dipoles in the T_0 tetrahedron while the line at 125.0 cm^{-1} – by this dipoles in the T_1 one and very small line at 128.6 – in the T_2. So, the frequency consequence takes place for HgTe-like modes: ${}^{HgTe}\omega_0 < {}^{HgTe}\omega_1 < {}^{HgTe}\omega_2 < {}^{HgTe}\omega_3$ according with work of Kozyrev et al. [10]. Analogical analyses for CdTe-like modes shown that the line at 151.5 cm^{-1} is generated by Cd-Te dipoles in T_1 tetrahedron and the line at 147.3 cm^{-1} – by the same dipoles in T_2 one. The frequency consequence for CdTe-like modes is: ${}^{CdTe}\omega_1 > {}^{CdTe}\omega_2 > {}^{CdTe}\omega_3 > {}^{CdTe}\omega_4$ what agree with the data of work [10] also. It allow to find to what basic cells (tetrahedra) belongs each observed vibrational mode generating by Hg-Te and Cd-Te dipoles: corresponding tetrahedra are shown in Fig. 5 for CPM (T_n) as well as for APM (T_{nv}).

The general description of the phonon spectra is based on Fig. 5 where the composition dependences of the mode frequencies at the room temperature are present. In the MCT lattice there are two positions for Hg-atoms: stable one (Hg^I) and metastable one (Hg^{II}) [4]. If temperature increase, the number of Hg-atoms occupied the meta-stable positions (Hg^{II}) increases also and the deformation of crystal lattice rises, respectively. The last factor can cause the removing of degeneracy of the HgTe-like CPMs in *n-$Hg_{0.8}Cd_{0.2}$ Te* when the temperature increases over the 100 K: the AVMs appear simultaneously, too. Indeed, the AVM at 112 cm^{-1} (beside very weak from 30 K at 108 cm^{-1}) take place after 100 K in n-type $Hg_{0.8}Cd_{0.2}Te$ and after 200 K appear additionally one

AVM at 115-116 cm^{-1}. The presence of Hg^{II} in a tetrahedron leads to the stretching of bonds which in its turn causes the shift of the *Hg-Te* oscillation frequency towards smaller frequencies. This effect can occur in three kinds of tetrahedra: 1) containing *3 Hg*-atoms in stable position (Hg^{I}) and one Hg^{II} *;* 2) containing two Hg^{I}, one Cd-atom and one Hg^{II}; 3) containing one Hg^{I}, two *Cd*-atoms and one Hg^{II}. The frequencies of *Hg-Te* oscillations in these tetrahedra should be arranged in the next sequence: the lowest frequency corresponds to the *Hg-Te* oscillations in the tetrahedron of first type and most higher corresponds to the oscillations in the tetrahedron of third type.

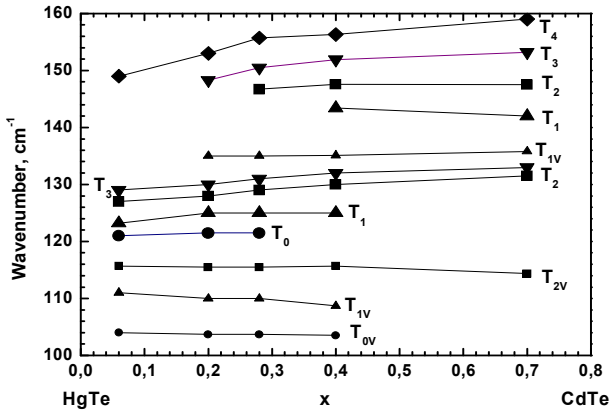

F

Fig.5.The composition dependencies of the phonon mode frequencies for *p-*$Hg_{1-x}Cd_x$ *Te,* at temperature 300K.

The lines in the range of 135 -137cm^{-1} are generated as could be assumed, by the oscillation of *Cd -Te* pair in the tetrahedra containing two Hg^{I}, one *Cd*-atom and one Hg^{II}.

Therefore, the Figure 5 enable us to assume that the phonon spectra in *MCT* are reproduced in two versions: first one is realized in the lattice consisted only from the Hg^{I}-atoms (that are *CPM*) and second one occurs in the lattice included the Hg^{II}-atoms too (that are *APM*).

In Fig. 6 are shown the values of the oscillator strengths sums (OSS) for the Hg-Te dipoles and for Cd-Te dipoles for each samples investigated. The data are presented in two way: i) only OSS for CPMs are included (open circles and squares), for x=0.2 there are two open circles because first one (upper open circle) is regarded to *n-*$Cd_{0.2}Hg_{0.8}Te$ and lower open circle – to *p-*$Cd_{0.2}Hg_{0.8}Te$; ii) in the OSS are included the APM OSS also (filled circles and squares). That enable us to obtain the dependencies of the OSS on composition. As follow from Fig. 6 if the oscillator strengths of APM are included in the sum of the oscillator strengths for the modes generated by Hg-Te dipoles as well as Cd-Te dipoles the OSS are proportional to the contain of correspond compound: to the

x in case of Cd-Te dipoles and to the *1-x* in case of Hg-Te ones. As was mentioned above (see Eqns. (8) and (10)) these dependences are considered as a criterion of applying the Bernoulli equation to the phonon spectra interpretation of the ternary solid solutions.

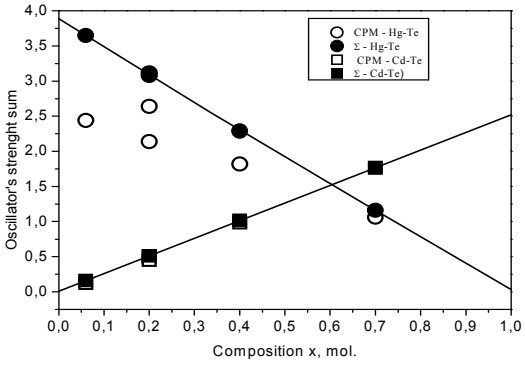

Fig.6. The oscillator strength sum dependence on composition for the HgCdTe alloys

By this way, the same model developed for the quaternary alloys enable us successfully explain observed structure of the sub-bands for the $Zn_xCd_yHg_{1-x-y}Te$ alloys [11].

Table 2. The oscillator strength sum for Zn-Te dipoles in measured samples of $Zn_xCd_yHg_{1-x-y}Te$.

x, mol	OSS for Zn-Te
0.02	0.065
0.05	0.197
0.07	0.211
0.12	0.769
0.18	0.907

The next step is calculation of the OSS for certain dipole pairs. It is reason to consider the dependence on composition of the OSS for Zn-Te dipoles (the ZnTe contain is changed from 0.05 to 0.18). In Table 2 are shown calculated OSS for this dipoles. From Table 2 follow that really OSS for Zn-Te dipoles approximately is proportional to contain x of ZnTe in the $Zn_xCd_yHg_{1-x-y}Te$ alloys. Therefore, this important consequence of the random model (Eqn.17) is fulfilled.

4. Conclusions

The results described above for HgCdTe and HgZnCdTe can give affirmative answer on the question: whether geometry of chaos e.g. the Bernoulli equation is enough to describe the observed phonon spectra of ternary and quaternary alloys. The main criterion of the random distribution of atoms in the solid solution lattice – proportionality of the oscillator strength sum for the

each dipole pair to the content of the corresponding component – is fulfilled if the observed additional modes will be involved in sums of the oscillator strengths.

Application of the Bernoulli equation to the ternary and quaternary alloys enable us to decipher the tangled phonon spectra in these case of semiconductor solid solutions.

References

1. Taylor D.W. in: Elliot R.J., Ipatova I.P. (Eds), *Optical properties of mixed crystals*, Elsevier Science Publishers, Amsterdam, pp. 35-131, 1988.
2. Ziman J.M., *Models of disorder*, Cambridge University Press, Cambridge, England, 1979
3. Robouch B., Kisiel A. and Sheregii E. M., *Phys. Rev B*., **64,** 073204 (2001)
4. Polit J., E.M. Sheregii, J. Cebulski, A. Marcelli, B. Robouch, A. Kisiel, A. Mycielski, *Phys. Rev. B*, **82**, 014306 (2010).
5. Sheregii E. M, *Infrared Spectroscopy*, v.2, ed.T. Theophanides, INTECH, 2012, pp. 467-492.
6. Cestelli Guidi M., Piccinini M., Marcelli A., Nucara A., Calvani P., Burattini E., *Journal of the Optical Society of America*, **A22,** 2810 (2005)
7. Baars J. and Sorgers F., *Solid State Commun*.**10,** 875 (1972)
8. Amirtharaj P.M.,. Dhart N.K, Baars J. and Seelewind H., *Semicond. Sci. Technol.* **5,** S68 (1990)
9. Rath S., Jain K.P., Abbi S.C., Julien C., Balkanski M., *Phys . Rev. B* ,**52,** 24, 17172 (1995)
10. Kozyrev S.P., L.K. Vodopyanov, R.Triboulet, *Phys. Rev. B,* **58**, 3, 1374 (1998)
11. Sheregii E.M., J.Polit , J. Cebulski, A. Marcelli, M. Castelli Guidi, B. Robouch, P. Calvani, M. Piccini, A. Kisiel, I. V.Ivanov-Omskii, *Infrared Physics & Technology* **49**, 13 (2006)

Chaotic Modeling and Simulation (CMSIM) 2: 153-160, 2014

Nonlinear reply of radon and deterministic chaos

Miraç Kamışlıoğlu[a], Fatih Külahcı[a], Fatih Özkaynak[b]

[a]Fırat University, Faculty of Science, Department of Physics, Nuclear Physics Division, Elazig, TR-23119, Turkey.
[b] Fırat University, Department of Software Engineering, TR-23119 Elazig, Turkey.
E-mails: m.kamislioglu@gmail.com ; fatihkulahci@firat.edu.tr

Abstract: Many studies have been achieved in applied sciences on the earthquake prediction by researchers. The chaotic non-linear structural behaviour of earthquakes is well known. In order to understand the formation of seismic activity it is extremely important to record the continuous measurements of the soil radon gas (^{222}Rn). In this study, 2976 data of ^{222}Rn are used and the chaotic time series analysis is applied to ^{222}Rn data from the soil. Chaos theory provides a structured explanation for irregular behavior of ^{222}Rn and gas anomalies in systems that are not stochastic. Lyapunov exponents and correlation dimension method are used to show the existence of chaos time series. Chaotic behavior of ^{222}Rn has been showed. Application of methodologies is achieved for Gölcük Region, İzmit, Turkey, where it is seismically very active.

Keywords: Chaotic time series analysis; Chaotic modeling; Radon measurement; Chaos analysis.

1. Introduction

^{222}Rn exists from the layers of Earth and is created by the uranium deposits source in nature. Certain soils and rocks especially contain high levels of uranium, which is natural deposit of radon. The uranium is rich in structures like granite, phosphate, shale and pitchblende. Relations between ^{222}Rn-earthquake and movement of ^{222}Rn in the Earth layers and in the atmosphere have been searched serious [1, 2, 3, 4 and 5]. ^{222}Rn has a half-life of 3.82 days and it is an α-emitting noble gas, which is produced in the radioactive decay series of ^{238}U. ^{222}Rn tends to migrate from Earth layers to the surface of the Earth. The migration rate of ^{222}Rn, which is non-linear, depends on many factors such as the dispersal of the uranium in the soil and bed rock, porosity of soil, humidity, micro cracks, granulation, and such [6].

Okabe [1956] has indicated radon as an earthquake precursor and radon changes in atmospheric near surface and showed a favorable correlation with seismic activities. On the other hand, anomalously high radon concentrations of ground

Received: 6 August 2013 / Accepted: 15 April 2014
© 2014 CMSIM
ISSN 2241-0503

water have been associated with fault lines [7]. Radon is easily soluble in water and it diffuses into the groundwater and spring waters.
High concentration of radon is often found in soils overlying highly fractured rocks such as fault lines. Radon emanation increases during an earthquake [8, 9]. Radon levels, which are correlated with meteorological and hydrological data, and they are used successfully in the earthquake forecasting researches [10, 11].
In this study, 2976 data of the soil ^{222}Rn gas are used and the chaotic time series analysis by considerations of Lyapunov exponents and correlation dimension methods. The chaotic behavior of the ^{222}Rn concentration levels is determined. Finally, the results of the methodologies are achieved for Gölcük Region (Turkey).

2. Methodology and Research Area

The methodologies which are used in this study are based on the chaos theory. It is aperiodic long-term behavior in a deterministic system that exhibits sensitive dependence on initial condition and disorder behaves in an unexpected way [12]. Likewise, it depends on structure of the system as well as by certain parameters and is usually unstable, complex and non-linear systems are emerging [13].
Determination of the chaotic behavior in the natural events' behaviors is very difficult; therefore, chaos theory is a suitable tool to show the characteristic of the dynamical system.
The chaos methodologies are applied to data recorded at Gölcük Region located on the North Anatolian Fault Zone (NAFZ). ^{222}Rn data are recorded between from 01/05/2006 to 31/05/2006 dates. It is continuously measured from the soil at 15 min intervals for a month.

3. Results and Discussions

3.1. Chaotic Time Series Analysis

Chaotic time series are unpredictable systems. These systems contain large complexity. Prediction of non-linear time series is an available method to appraise characteristic of dynamical systems [14].
Chaotic time series analysis methods are most enforceable in cases where the data include nonlinearity. The first of these analysis methods is obtained as the degree of non-linear positive Lyapunov exponents [15].
If these methods display irregular or unpredictable behavior, then it is called chaotic. On the contrary, it is called non-chaotic. Fig. 1 shows the time series of chaotic behavior of ^{222}Rn data taken from Gölcük Region on NAFZ. Non-linear time series analysis starts from measured experimental time series of $x_1(t), x_2(t), \Lambda\ , x_n(t)$, at n points. The same analysis provides various tools to determine the temporal structures embedded in the time series.

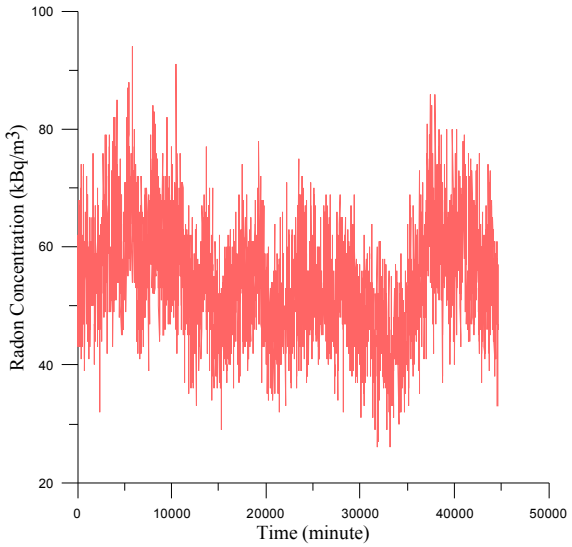

Fig. 1. Time series state variable for chaotic behavior

3.2. Lyapunov Exponent

Lyapunov exponents can be defined as the exponential increase or decrease of minor perturbations on an attractor. Largest Lyapunov exponent is one of the most practical methods to define chaotic behavior in a system [16]. The basis of Lyapunov exponent is very close to each other to monitor both the starting point, which is based on very different trajectories. Its sign gives information about the system dynamics. When exponential value is positive, system indicates chaotic behaviours. This condition, on initial conditions of the system, shows sensitive dependence [17]. The largest Lyapunov exponent can be anticipated in accordance with the algorithm Wolf et al. [18]. These applications are valid between neighboring points in the reconstructed phase space algorithm. In the following, the results have been shown concerning the maximum Lyapunov exponents (L_{max}), where $t \to \infty$, $d(0) \to \infty$ and $d(t)$, and hence, show the difference between two measurements. Largest Lyapunov exponent is calculated according to the following expression. The result is given for the ^{222}Rn data in Fig. 2.

$$L_{\max} = \lim \left[\ln \left[\frac{d(t)}{d(0)} \right] \right], \tag{1}$$

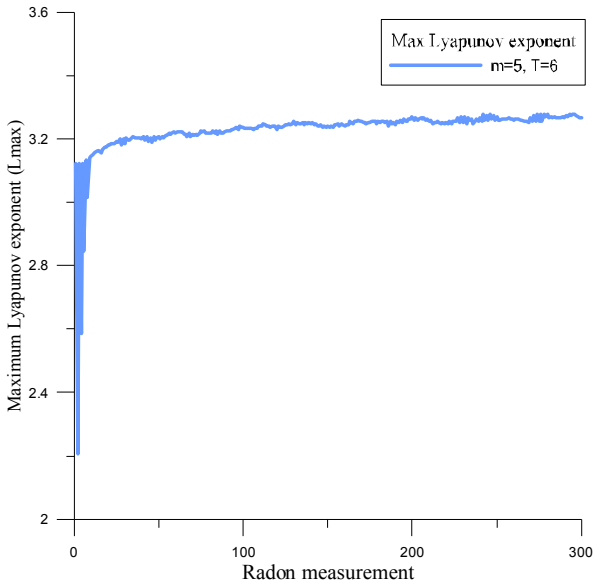

Fig. 2. Lyapunov exponent for ^{222}Rn (m: embedding dimension; τ: delay time)

3.3. Hurst Exponent

Hurst exponent is used to predict from time series [19]. Hurst exponent coefficient is an additional statistical measure necessary for the classification of time series. Hurst exponent calculation is explained also through the Rescaled range, R/S analysis, where R is the range of the accumulated data and S is the standard deviation. This exponent, H, can change between 0 and 1. Its calculation is possible from the discrete time series data set $\{x_t\}$ of dimension N by computing the mean, $\bar{x}(N)$ and standard deviation, $S(N)$ leading to,

$$\bar{x} = \frac{1}{N}\sum_{t=1}^{N} x_t \tag{2}$$

and

$$S(N) = \left[\frac{1}{N}\sum_{t=1}^{N}(x_t - \bar{x}(N))^2\right]^{1/2} \tag{3}$$

respectively. Range of cumulative departures of the data is given by $R(N) = \max\{X(n,N)\} - \min\{X(n,N)\}$

Finally, the Hurst exponent can be calculated as follows,

$$\langle R/S \rangle \cong (n)^H \tag{4}$$

If Hurst exponent is equal to 0.5, then it shows a random walk. A Hurst exponent between 0.5 and 1 proves the presence of chaos in the system. With

the data at hand, it is computed as 0.56 for ^{222}Rn data from Eq. 4 and the results are given in Fig. 3.

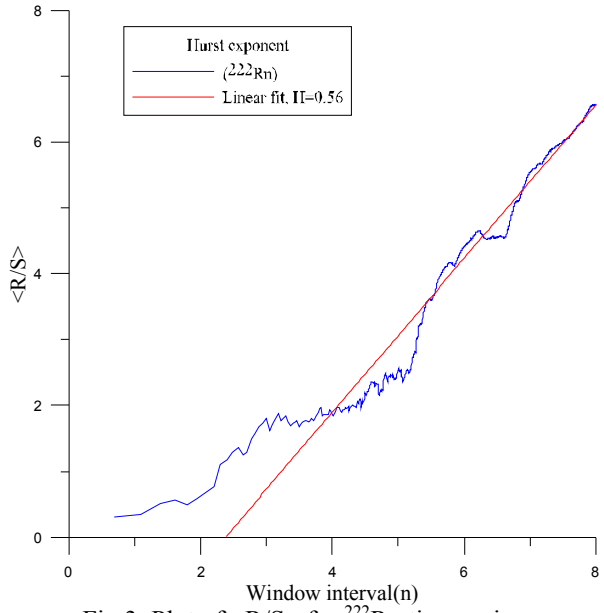

Fig.3. Plot of <R/S> for ^{222}Rn time series

3.4. Correlation Dimension

Correlation dimension is used to determine the degree of chaotic behaviour in a signal or time series. That is, correlation dimension, D_2, aids to determine whether a signal behaves like a random or chaotic distribution. The algorithm, measure of D_2 has presented by Grassberger- Procaccia [20]. These dimensions need to compute the correlation integral. Correlation integral function $C(r)$ can be defined as follows,

$$C(r) \approx \lim_{N\to\infty} \frac{1}{N^2} \left\{ \left| x_i - x_j \right| \le r \text{ the number of pairs } (i,j) \text{ which statement} \right\} \quad (5)$$

$$C(r) = \lim_{N\to\infty} \frac{1}{N^2} \times \sum_{i=1}^{N} \sum_{j=i+1}^{N} H(\left| x_i - x_j \right| \le r) \quad (6)$$

The distance between two units with (such as, x_i and x_j) Euclidean definition can be computed as,

$$\left| x_i - x_j \right| = \sqrt{\sum_{k=1}^{m} (x_i(k) - x_j(k))^2} \quad (7)$$

H is the Heaviside step function, which can be expressed as follows.

$$H(x)=\begin{cases}1, & x\geq 0,\\ 0, & x\leq 0,\end{cases} \tag{8}$$

If the system is chaotic, then D_2 will be the largest value. Kaplan and Yorke study showed correlation of Lyapunov exponents of information dimension [21]. D_2 can also be calculated as follows.

$$D_2=\lim_{r\to 0}\frac{\log C(r)}{\log(r)} \tag{9}$$

In this study, one can draw $\log C(r)$ as a function of $\log(r)$ and compute D_2 from the slope of a linear fit. Embedding dimensions corresponding to the correlation dimensions for a period of chaotic deterministic process are shown in Figure 4. Also, for ^{222}Rn correlation dimension, D_2, is given in Fig. 4. Time scale of dynamical system is similar to the D_2 values' mutual predictions. Values of the embedding dimension are given resource about the change of $C(r)$.

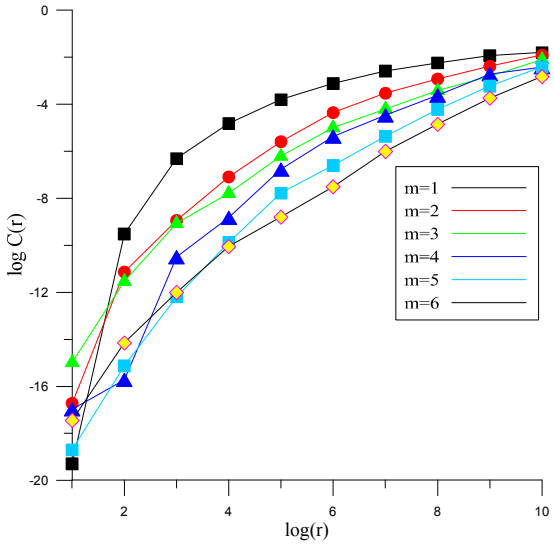

Fig. 4. The estimate of correlation dimension for ^{222}Rn time series

4. Conclusions

Natural and geophysical observations are not regular usually. Chaotic analyses are useful tools to describe the natural irregularity. In this study, they are used as chaotic methods. The non-linear behaviour of ^{222}Rn in the Earth layers is showed. The chaos methodologies in order to show non-linear behaviour of

^{222}Rn are applied to ^{222}Rn data taken from the Gölcük Region on the North Anatolian Fault Line. The soil ^{222}Rn gas, which propagates from the fault lines, has a nonlinear characteristic.

Acknowledgements

This research is supported by Republic of Turkey Prime Ministry Disaster & Emergency Management Presidency (AFAD). We especially would like to thank Dr. Murat Nurlu and Bengi Eravcı from AFAD and Prof.Dr. Zekâi Şen from İstanbul Technical University for support and encouragement.

References

1. A.B. Tanner. Physical and chemical control on distribution of radium-226 and radon-222 in ground water near Great Salt Lake, Utah, in The Natural Radiation Environment, edited by J: A. S. Adams and W. M. Lowder, pp. 253-276, University of Chicago Pres, Chicago,1964.
2. S. Uyeda, T. Nagao, M. Kamogawa. Short-term earthquake prediction: Current status of seismo-electromagnetics. Tectonophysics vol. 470, pp. 205-213, 2009.
3. H.S. Virk, B. Singh. Radon anomalies in soil gas and groundwater as earthquake precursor phenomena. Tectonophysics vol. 227, pp. 215–224, 1993.
4. M. Trique, P. Richon, F. Perrier, et al. Radon emanation and electric potential variations associated with transient deformation near reservoir lakes. Nature vol. 399, pp. 137-141, 1999.
5. J. Planinić, V. Radolić, B. Vuković. Radon as an earthquake precursor. Nucl Instrum Methods vol. 530, pp. 568-574, 2004.
6. M.H. Al-Tamimi and K.M. Abumurad. Radon anomalies along faults in North of Jordan. Radiat. Measur., vol. 34, pp. 397-400, 2001.
7. M.M. Moussa, A. –G.M. El Arabi. Soil radon survey for tracing active fault: a case study along Qena-Safaga roadCC Eastern Desert, Egypt. Radiat. Meas. vol. 37, pp.211-216, 2003.
8. V.I. Ulumov, B.Z. Mavashev. Forerunners of the Tashkent earthquake. Izv. Akad. Nauk Uzb. SSR, pp 188-200, 1971.
9. G. Igarashi, S. Saeki, N. Takahata, K. Sumikawa, S. Tasaka, Y. Sasaki, M. Takahashi, Y. Sano. Ground-water radon anomaly before the Kobe earthquake in Japan, Science, vol. 269, pp. 60–61,1995.
10. F. Külahcı, M. İnceöz, M. Doğru, E. Aksoy, and O. Baykara. Artifical neural network model for earthquake prediction with radon monitoring. Appl. Radiat. Isot., vol. 67, pp. 212-219, 2009.
11. C.Y. King. Radon monitoring for earthquake prediction in China. Earthquake Pred. Res. vol. 3, pp. 47-68, 1985.
12. G.L. Baker, J.P. Gollub. Chaotic Dynamics an Introduction, Cambridge University Press, 1990.
13. K. Giannakopoulos, T. Deliyannis, J. Hadjidemetriou. Means for Detecting Chaos and Hyperchaos in Nonlinear Electronic Circuits,. DSP vol.2, pp. 951-954, 2002.

14. J. Zhang, K.F. Man. Time series prediction using recurrent neural network in multi-dimension embedding phase space. IEEE International Conference on System, Man, and Cybernetics vol. 2, pp. 11-14, 1998.
15. I. Matsuba. Nonlinear time series analysis, Asakura, 2000.
16. C. Frazier, K.M. Kockelman. Chaos Theory & Transportation Systems: an Instructive, Transportation Research Record vol. 1897, pp. 9-17, 2004.
17. A.B. Özer, E. Akın, Tools for Detecting Chaos, SAÜ Inst. Science Magazine, vol. 9, pp. 60-66, 2005.
18. A. Wolf, et al. Determining Lyapunov exponents from a time series. Phys D, vol. 16, pp.285-317, 1985.
19. C.M. Harris, R.W. Todd, S.J. Bungard, R.W. Lovitt, J.G. Morris, D.B. Kell. The dielectric permittivity of microbial suspensions at radio- frequencies: a novel method for estimation of microbial biomass, Enzyme Microbial Technology. vol. 9, pp. 181-186, 1987.
20. P. Grassberger, I. Procaccia. Characterization of strange attractors. Phys. Rev. Lett. vol. 50, pp. 346-349, 1983.
21. J. Kaplan, J. Yorke. Fuctional Differential Equations and the Approximation of Fixed Points. Lecture Notes in Mathematics, No 730, Berlin: Springer Verlag, 1979.

Chaotic Modeling and Simulation (CMSIM) 2: 161-177, 2014

Behavioral Modeling of Microtweezer Integrated with Capacitive Touch Sensor

Nayyer Abbas Zaidi[#1], Shafaat A. Bazaz[#2], Nisar Ahmed[#3], Rahim Umar[#4]
[#1#,3] Faculty of Electronic Engineering, Ghulam Ishaq Khan Institute of Engineering Sciences and Technology, Pakistan.
[#2]Department of Computer Science, Centre for Advance Studies in Engineering (CASE), 19 Ataturk Avenue, G-5/1, Islamabad, Pakistan.
[#4] Faculty of Engineering Sciences, Ghulam Ishaq Khan Institute of Engineering Sciences and Technology, Pakistan.
E-mail: nayyergiki@gmail.com

Abstract: This paper presents behavioral modeling of an electrostatic microtweezer integrated with capacitive touch sensor. The design of the microtweezer is optimized using standard SOIMUMPS process. Microtweezer performance is forecasted using system level simulation. The results of the system level simulation obtained from behavioral modeling shows total displacement of 7.039 µm and 37.5 µm is obtained at central beam and tweezer jaw respectively, when a voltage of 55 V is applied. Behavioural modeling of the sensor part of microtweezer is performed and system level simulation results shows that minimum and maximum capacitance is 0.45 pF and 0.65 pF respectively. Pull-in voltage analysis through behavioral modeling shows that actuator works with maximum performance, at applied voltage of 55 V. The results of displacement, sense capacitance and pull-in voltage analysis are nearly identical to analytical results when compared.

Keywords: MEMS, Behavioural model, SOIMUMPS, System level simulation, Microtweezer..

1. Introduction

In the last ten years, new customized as well as standard micromachining processes have been emerged, making it possible to develop complex type of Microelectromechanical systems (MEMS). Due to such innovations, MEMS have found its place in many practical applications where one of the areas is micromanipulation of micro-objects. Micromanipulation has become important in the applications, like microassembly, to assemble parts of micron size that are generally fabricated on a substrate. One such micromanipulator was developed in 2004, that uses MEMS microtweezer as an end-effecter attached to the robotic workstation [1]. The microtweezer performs the task of grasping the micropart and then the robotic arm performs the manipulation operation. A passive microtweezer is designed to grasp the micro-object with a specific size. Another important application of micromanipulator is in the area of biological and biomedical research [2]. Design of three degree-of-freedom Micromanipulator based on MEMS heat actuators have been developed that can

Received: 4 August 2013 / Accepted: 8 April 2014
© 2014 CMSIM
ISSN 2241-0503

be used to probe or position biological object [3]. Another three degree-of freedom micromanipulator based on comb drive actuators were developed for precise positioning of probing instruments like Atomic Force Microscopy (AFM), or tools to provide energy beam like e-beam, X-ray etc. [4]. These systems cannot safely grasp the micro-objects. Moreover, all such systems do not provide integrated sensing mechanism that makes their use to limited applications.

Many MEMS based microtweezers have been proposed in recent years for different micromanipulation applications [2, 5, 6]. Most of these microtweezers were based on electrostatic or piezoelectric actuation principle. These microtweezers comprised of the jaws mechanism with the dimensions of the size of the cell that are generally of diameter of tens of microns. Moreover, these jaws should be able to grasp the cells with different and irregular shapes. In order to grasp more precisely, not only the jaw mechanism but also the integration of touch sensor, makes microtweezer design more effective. As this addition excludes the fracture of microobject due to the uncontrolled excessive force, which is not found in to the microtweezers design proposed by Kim and Volland [5, 6]. Finally, batch production of such system requires the use of standard MEMS based micromachining technology thus making it cost effective, have good repeatability and also reliability from the point of view of the fabrication and production of the microstructures.

To fabricate microtweezer, Modeling and Simulation plays vital role in predicting the dynamics of the device. These analytical and simulation results minimizes iterative fabrication that is costly and time consuming. Previously microtweezers were simulated using Finite Element Methods [2, 3, 19, 20]. Beside the fact that, these methods gave high accurate solution but a compromise is made in terms of times, memory requirement and the restriction of integration of electronics with the device, bounded the user to limited type of simulations.

On the other hand, Behavioral Modeling and system level simulation tool performs MEMS analysis efficiently both in terms of time, memory requirement and integration of electronics with the MEMS makes Microsystem to be analyzed in a single simulation environment. In mid-nineties, simulation tools such as SUGAR and NODAS that comprise basic MEMS elements library were developed at UC Berkeley and Carnegie Mellon University respectively, in which Matlab and Cadence are used as system level simulator [7, 8, 9]. Now days, very specialized MEMS modeling and simulation such as CoventorWare Architect [17] with large MEMS library is available to simulate MEMS devices. Various MEMS devices including Gas Sensors [10], Accelerometers [11] and Gyroscope [12] were first simulated in CoventorWare Architect and then they are fabricated.

This paper presents the analytical analysis of microtweezer with its novel behavioral modeling and simulation of both the actuator and the sensor part. In Section II, SOIMUMPs process is explained, in which sample model of the

microtweezer is designed. In section III, design details of microtweezer are explained. The theory of operation of microtweezer is explained in section IV. The parameters related to design such as displacement, change in capacitance and pull in voltage are discussed in section V. The behavioral modeling is illuminated in section VI and then results and discussion in section VII. Finally section VIII illustrates conclusion.

2. SOI-MUMPS Process

The standard SOI-MUMPs [13] process is selected for the development of sample model of microtweezer. The reason for choosing this process is, it is easily available with reliable design instructions. SOIMUMPs process offers, 2 μm minimum feature size and spacing between structure layers. This can be used to construct a high capacitance com drive. In order to grasp a microobject through microtweezer the grasping area should be equal or larger then the thickness of the micro-object. This process proposes quite high grasping area of 25 μm, which is enough to grasp a microobject. The fabrication sequence of the microtweezer using SOIMUMPs process is shown in Fig. 1.

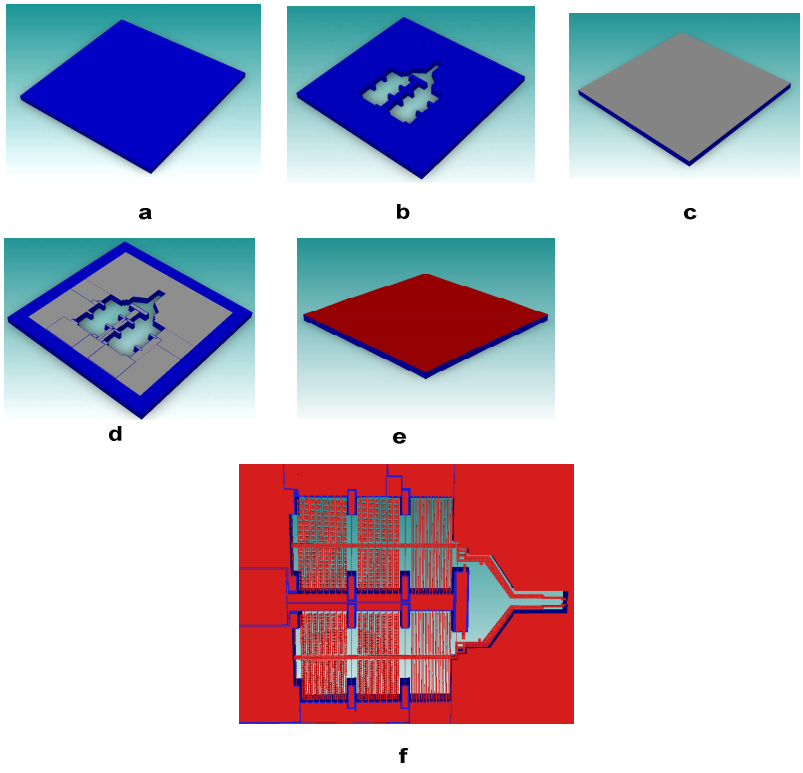

Fig. 1: Process flow for the fabrication of microtweezer using SOI-MUMPS in CoventorWare.(a)Silicon-on-insulator (SOI) wafer as starting substrate (b)DRIE silicon etch is used to etch substrate completely (c) Thermal

oxidation is done to built insulator layer on substrate (d) DRIE etch completely etch the substrate and oxide layer (e)Single crystal silicon layer is deposited having thickness of 25um (f) Deep reactive ion etch is used to etch the silicon to the oxide layer and after that finally DRIE is used to etch down to the oxide layer.

3. Microtweezer design

The designed microtweezer 2-D layout, developed in MEMSPro is shown in Fig. 2. It consists of three parts a) actuator b) sensor and c) jaws.

3.1 Actuator Design

The actuator part of the microtweezer is comprised of comb drive mechanism which is Lateral. This technique consists of interdigitated finger, in which fixed and moveable parts are called stator and rotor combs. The length of the fingers is set to 50 µm and overlap length is set to 30 μm. The spacing between the two fingers is designed to 3 μm to avoid the collapse of the fingers as shown in Fig. 3. The three clamped-clamped beams are used to suspend the structure and moves back the central mass movement to its free position.

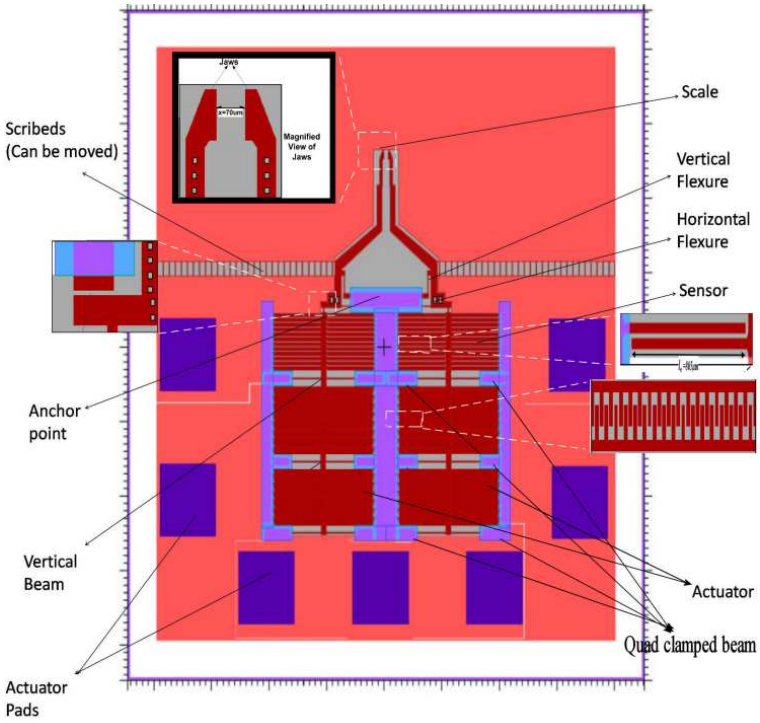

Fig. 2: Complete microtweezer design with integrated touch sensor.

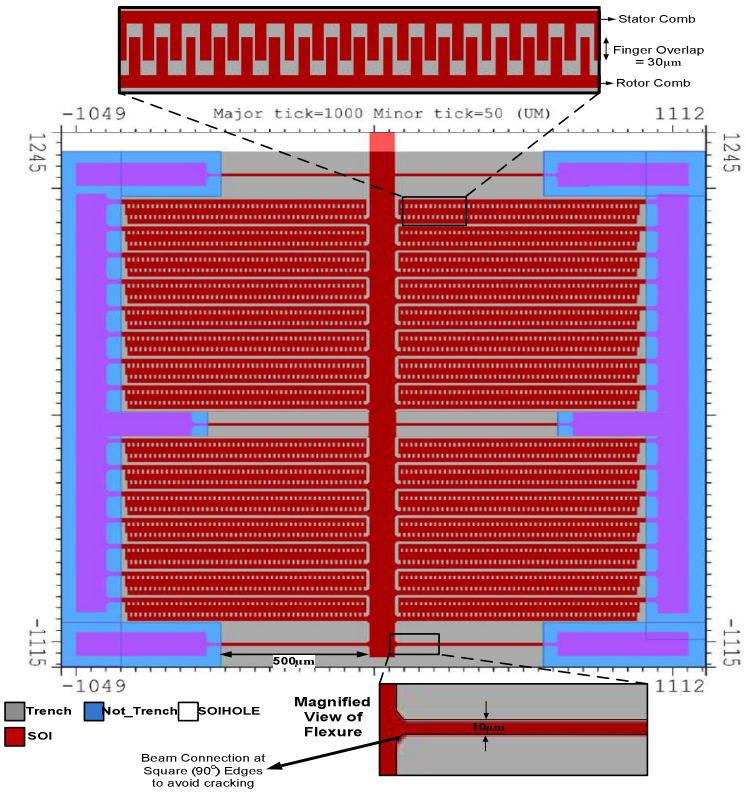

Fig. 3: Complete actuator design.

3.2 Sensor design

Differential transverse comb based touch sensor is designed to sense the touch when the object gripped between the tweezer jaws. The working principle of the sensor comb are, up on the application of the force applied to the moveable combs attached with the central mass cause the increase in the finger gap on one side of the microtweezer and decrease the same amount of gap on the other side of the moveable combs as shown in fig. 4. The overlap length and gap between the sensor fingers are 805 µm and 10 µm respectively and of the width of fingers is 25 µm.

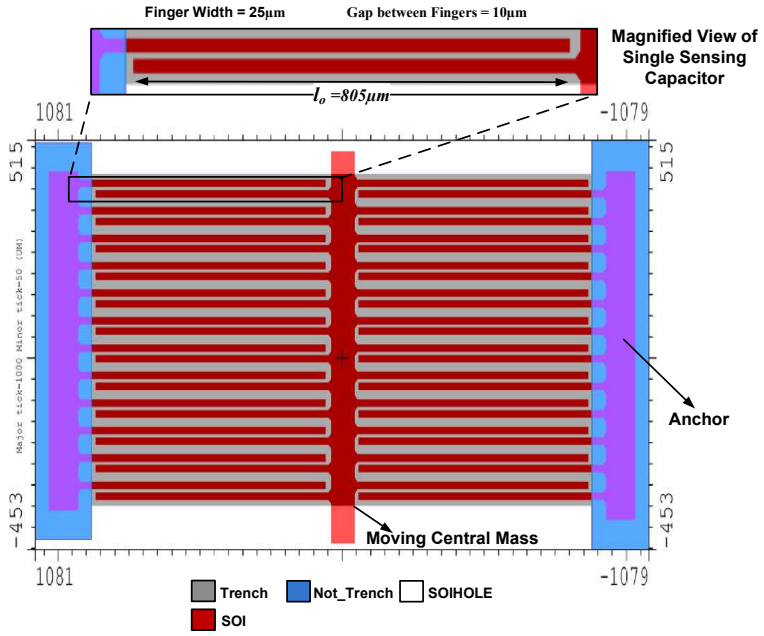

Fig. 4: Complete sensor combs design.

3.3 Jaw Design

A novel tweezer arm and jaw with the compliant structure has been designed as shown in Fig. 5 for grasping the micro-sized objects. The design includes a horizontal and a vertical beam to produce elastic restoring force in horizontal and vertical direction simultaneously. The vertical beam additionally provides support against the out of plane movement of the tweezer arms. The structure is designed in such a way that it will maintain an angle of 90^0 between the tweezer arm and the horizontal beam. Additionally, the jaw moves a little distance forward along *y*-axis during grasping due to direction of applied force. This action ensures that object completely comes between the jaws while grasping. Two stoppers have been placed near the point of application of force in order to stop any extra movement of central beam after the object has been fully grasped. In the proposed tweezer arm design, the vertical displacement produced in central beam is amplified by constant times the displacement produced at the tips of tweezer jaws.

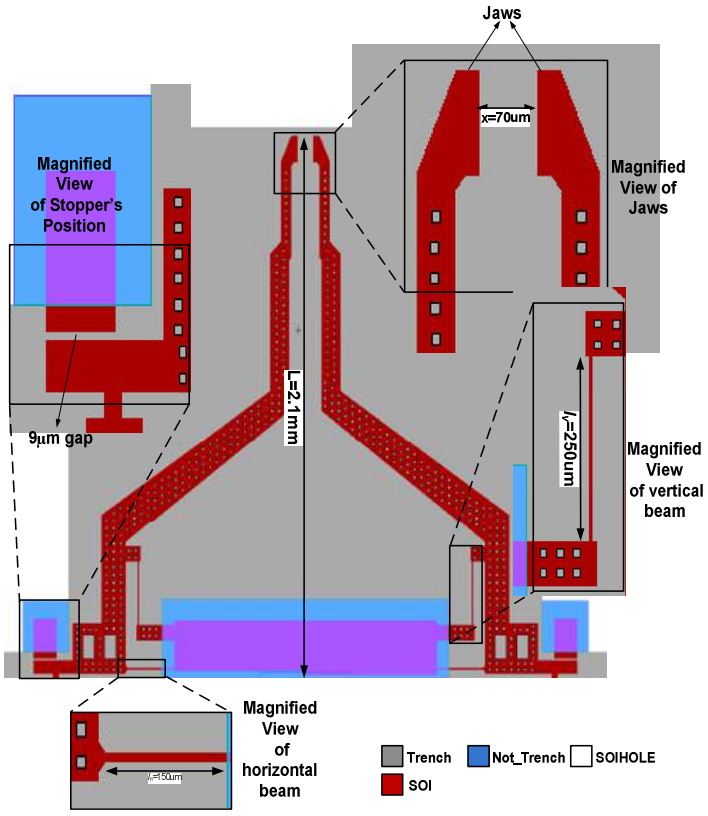

Fig. 5: Complete design of tweezer arms.

4. Theory of operation

The proposed microtweezer design uses novel dual electrostatic actuation system i.e. there are two separate electrostatic actuators for the simultaneous movement of two jaws. Each actuator consists of a set of stator combs interdigitated with a set of rotor combs. DC voltage is applied to both the actuators simultaneously such that the stator combs are at positive potential with respect to rotor combs. Hence electrostatic force is produced which pulls the two comb drives. This electrostatic attraction produces elastic restoring force in the quad clamped flexure springs which is equal in magnitude to the applied force. The central beam of each actuator is attached to the respective tweezer arm. Each tweezer arm is further supported by two cantilever beams namely horizontal and vertical beam. Hence total elastic restoring force is a combination of force due to the quad-clamped flexure springs and the two cantilever beams. Any vertical movement of the central beam in upward direction is amplified at the tweezer jaws due to the integrated action of the tweezer arm and the beam

system. One transverse comb drive based capacitive touch sensor is included along each of the two central beams in between the tweezer arm and actuator explain in Fig. 2. The overlap length varies in the sensor combs result in the change in capacitance. When there is no capacitance change it indicates that the object has been gripped and thus to avoid any damage to the object no further actuation voltage is applied.

5. Design parameters

5.1 Displacement of central beam

An applied voltage to actuator generates electrostatic force between the comb drives. This electrostatic force is conveyed to the jaw via quad-clamped, horizontal and vertical flexures. The spring constant of flexures added because of parallel connection [15].

$$K = k_h + k_f + k_v \tag{1}$$

$$K = Et\left(\frac{8b_f^3}{l_f^3} + \frac{b_h^3}{4l_h^3} + \frac{b_v^3}{4l_v^3}\right) \tag{2}$$

Using Hook's law force in terms of displacement is given as:

$$F = Et\left(\frac{8b_f^3}{l_f^3} + \frac{b_h^3}{4l_h^3} + \frac{b_v^3}{4l_v^3}\right) \text{EMBED Equation.3 } y \tag{3}$$

The electrostatic F produced by actuator is given as:

$$F = \frac{N.n}{2}\varepsilon\frac{tV^2}{d} \tag{4}$$

Where nN is the entire number of comb drives connected in parallel, t is the thickness, d is the gap between the comb drives and V is the applied voltage. Eq. (3) and (4) are equated, the central mass displacement is given as:

$$y = \frac{\frac{N.n}{2}\varepsilon_o\frac{tV^2}{d}}{Et\left(\frac{8b_f^3}{l_f^3} + \frac{b_h^3}{4l_h^3} + \frac{b_v^3}{4l_v^3}\right)} \tag{5}$$

5.2 Displacement of single Jaw

The horizontal flexure and the length of the jaw are responsible for the amplification at the jaws. Thus central beam movement is amplified by L/L_Q. The total movement at single jaw is calculated as:

$$X = \frac{L}{l_Q} \boxtimes \text{EMBED Equation.3} \boxtimes\boxtimes\boxtimes \frac{\frac{N.n}{2}\varepsilon\frac{tV^2}{d}}{Et\left(\frac{8b_f^{\,3}}{l_f^{\,3}}+\frac{b_h^{\,3}}{4l_h^{\,3}}+\frac{b_v^{\,3}}{4l_v^{\,3}}\right)} \tag{6}$$

Where $L=2.1mm$ is the length of the microtweezer jaws and $l_Q = 150\ \mu m$ horizontal flexure length as shown in Fig. 5.

5.3 Sensor

In the sensor, the capacitance increases and decreases by same proportion on the two sides of the comb drives. These capacitances are given as:

$$\left.\begin{aligned} C_{s1} &= Nn\frac{\varepsilon(t\times l)}{d_0+\left(\frac{L}{L_Q}\right)X}+C_{fringe}\\ C_{s2} &= Nn\frac{\varepsilon(t\times l)}{d_0-\left(\frac{L}{L_Q}\right)X}+C_{fringe}\end{aligned}\right\} \tag{7}$$

where d_0 is the initial gap between the transverse combs, C_{s1} is the decreased capacitance and C_{s2} is the increased capacitance in the transverse comb sensor corresponding to the gap change $y=\left(\frac{L}{L_Q}\right)X$ and C_{fringe} is the capacitance produced due to the fringe fields.

5.4 Pull-in Voltage

In the proposed microtweezer design, the comb drive actuator one of which, typically called as rotor finger, is suspended and connected to the compliant springs while other, usually called as stator finger, is fixed. The pull in voltage is defined as the voltage at which the two fingers come in touch with each other. The pull-in voltage $V_{pull\text{-}in}$ is given [16]:

$$V^2_{pull-in} = \frac{d^2k_y}{2\varepsilon_0 bn}\sqrt{2\frac{k_x}{k_y}+\frac{y_0^{\,2}}{d^2}}-\frac{y_0}{d} \tag{8}$$

Where d is the gap spacing between the fingers, ε_o is the dielectric constant in air, $\frac{k_x}{k_y}$ is the spring stiffness ratio.

6. Behavioural model development

The reduced order equations are used to perform behavioral modeling and simulation. In this modeling technique complete model is simulated rather than simulating number of finite components that constitute the model. Thus the efficiency in time is achieved in this method rather than finite element analysis. The components that are used to develop behavioral model are presents in its libraries. The core code inside these libraries tells the individual components how to behave when exposed to stimuli in terms of electrical and mechanical [17]. The main components that develop behavioral model design are Beams, Comb drives and rigid plates. Fig. 6 shows the behavioral schematic of the actuator, sensor and jaw. Mechanical bus is used for connecting the components. This bus consists of array of six wires in which three are translational and other rotational. These wires contain information about rotational and translational motion of the mechanical components in space. The mechanical bus connector is connected at the tip of the jaw and with central beam in order to find their displacement. The 3-D model shown in Fig. 7 is generated after net listing and importing the schematic design in to scene 3D of the architect. In the 3D model half portion of the microtweezer is modeled because of geometrical evenness.

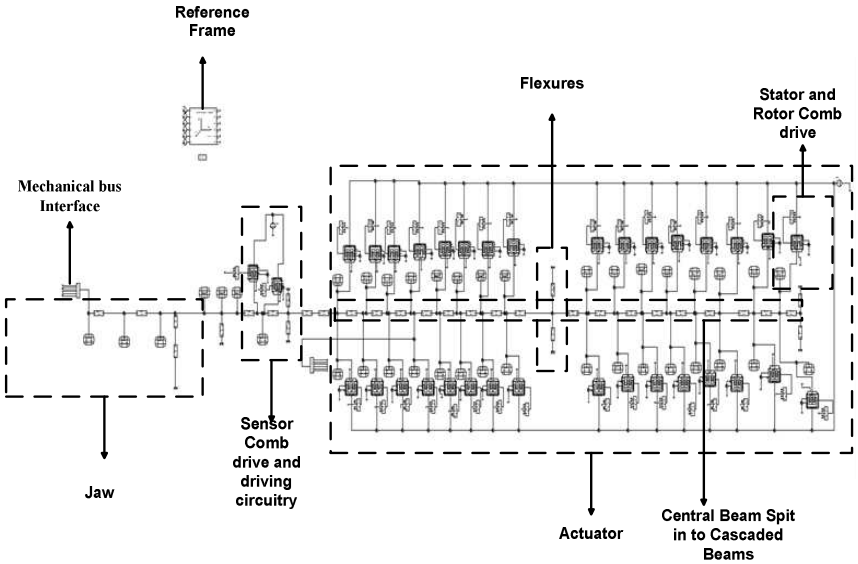

Fig. 6: Behavioural schematic of the microtweezer.

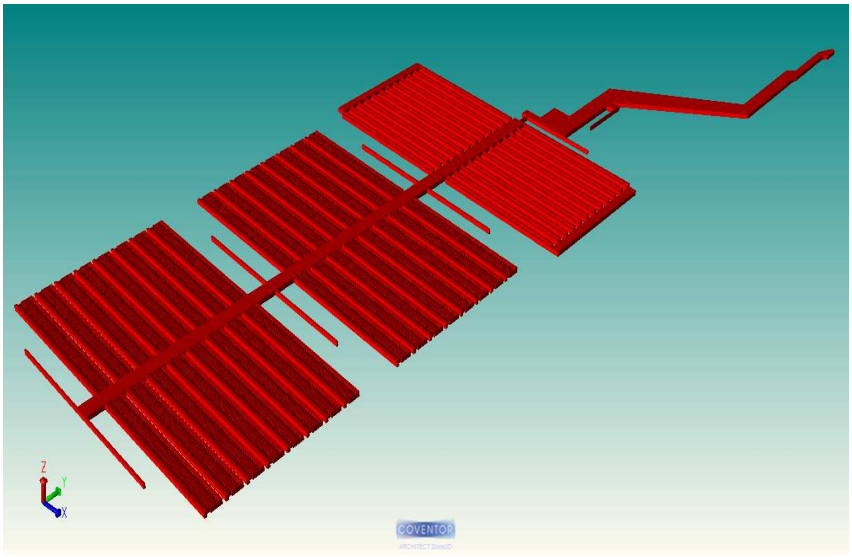

Fig. 7: Microtweezer 3-D model in CoventorWare architect.

7. Result & discussion

The graph shown in Fig. 8 obtained analytically (by Eq. (5)) for a displacement of central beam when a voltage is sweep form 0 - 55 V. At 50 V the displacement is found to be 6.3 μm. The behavioral model simulation, between voltage and central beam displacement is shown in Fig. 9. Both the results are approximately same as analytically predicted. The simulation results are shown in Fig. 10, the color of the contours plot shows the displacement of every component of the microtweezer in y-axis direction. It is observed that stator combs are stationary while rotor combs moves the central beam in y-axis.

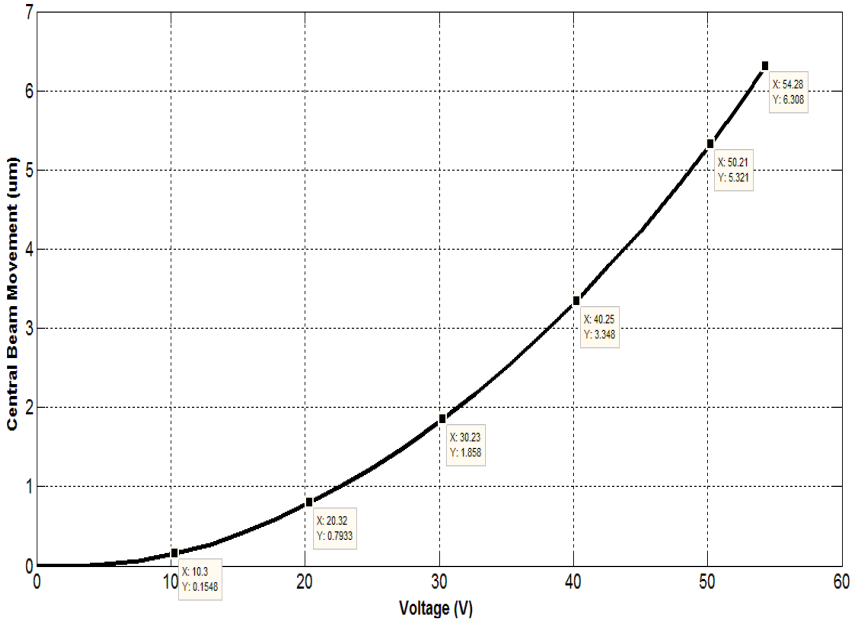

Fig. 8: Analytical relation between voltage (V) and central beam displacement (μm).

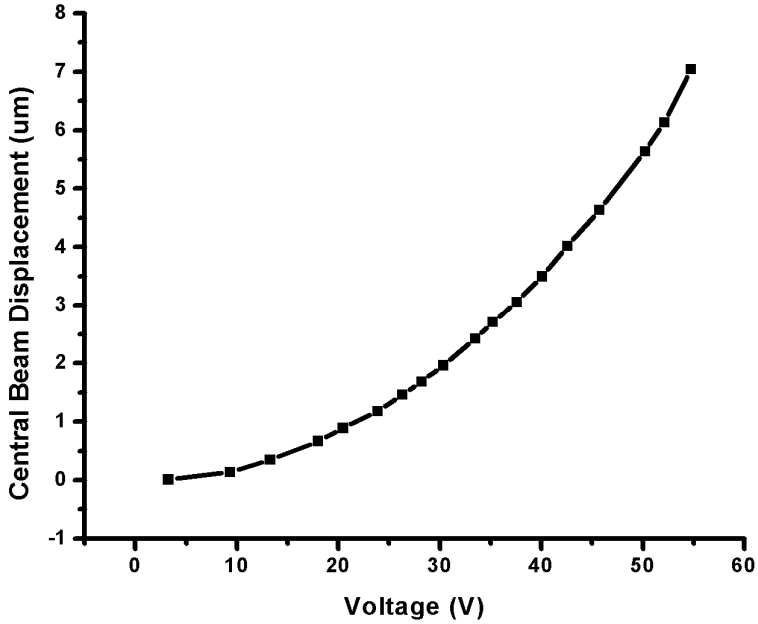

Fig. 9: Graph between voltage (V) and central beam displacement (μm) acquired by behavioral modeling.

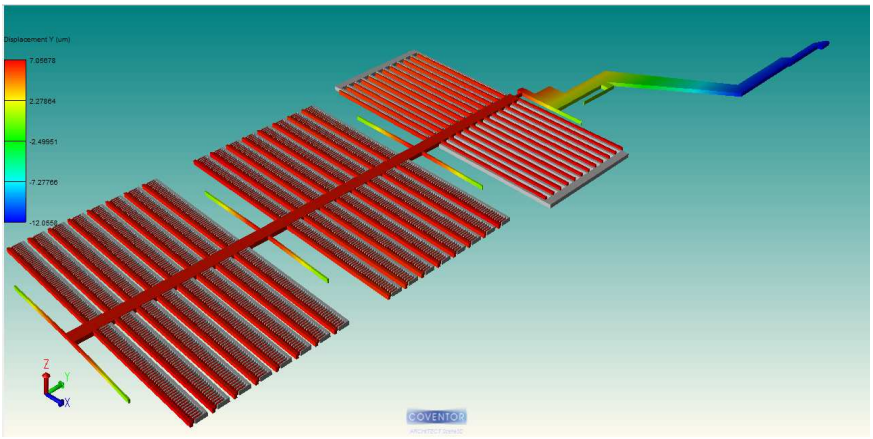

Fig.10: Displacement visualization in a color contours for microtweezer.

The graph shown in Fig. 11 is the analytically calculated result that is obtained from Eq. 6, between voltage (V) and the jaw displacement (μm). The maximum displacement obtained is at the tip of the jaw which is 34.3 μm at 55 V. The jaw displacement obtained through system level simulation is 38 μm at 55 V which is nearly same as analytically calculated. From analytically and simulation outcomes show that the microtweezer can easily grasp microobjects in diameter from 0 – 70 μm when it's both jaws are in motion. This can avoid the fabrication of 2 stage jaws [18].

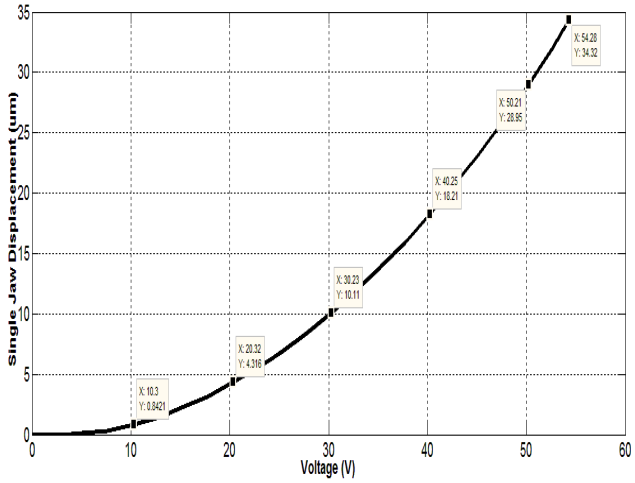

Fig. 11: Analytical relationship between voltage (V) and jaw displacement (μm).

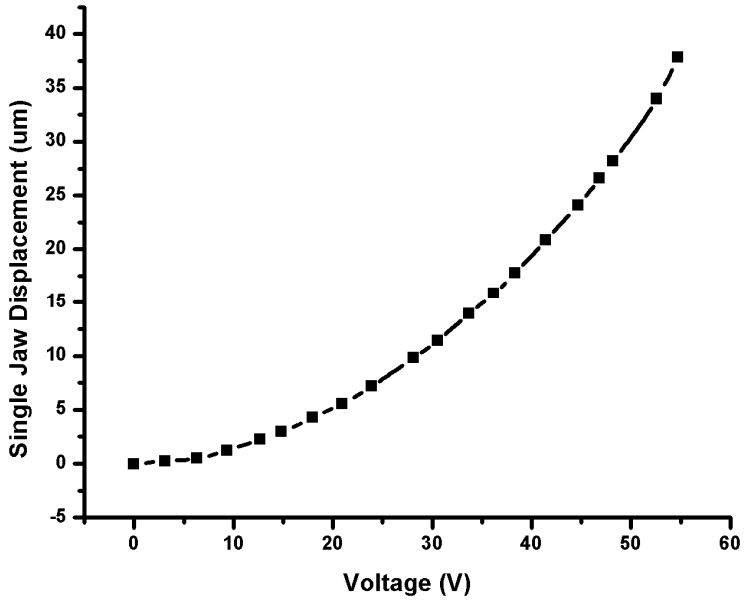

Fig. 12: Graph between voltage (V) and jaw displacement (µm) obtained by behavioral modeling.

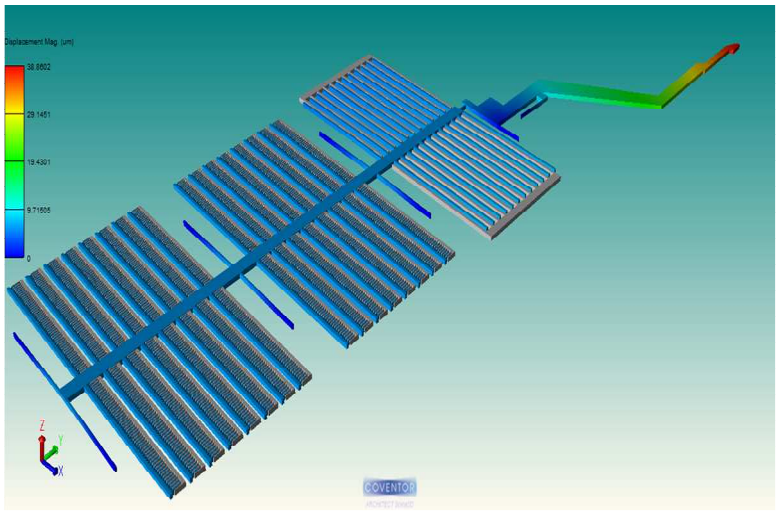

Fig. 13: Displacement visualization in a color contours for microtweezer.

The graph shown in Fig. 14 and Fig. 15 shows the change in capacitance vs displacement of transverse comb drive calculated both analytically by Eq. (7), and over behavioral modeling respectively. Form the result it is clear the capacitance on one side of the transverse C_{S1} increases while the capacitance on

the other end C_{S2} decreases. The behavioral model result shows the same capacitance increase and decrease. These results are approximately the same. The integration of the capacitive touch sensor informs that the range of capacitance (0.45 *f*F - 0.65 *f*F) that is obtained in gripping microobject. This range of capacitance is significant in programming the capacitive read out circuitry MS3110 [14].

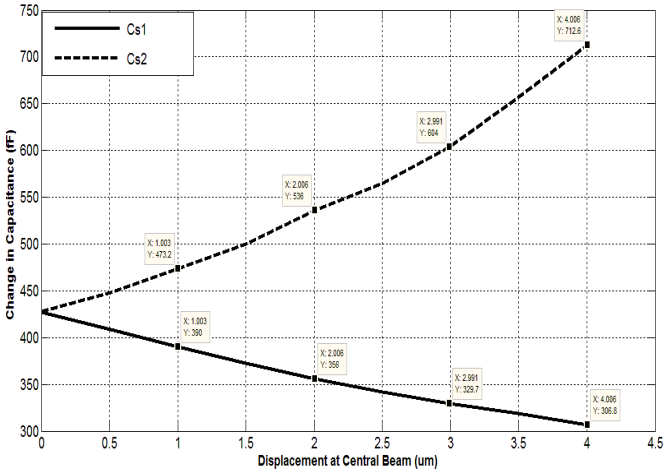

Fig. 14: Analytical relationship between displacement at central beam and change in capacitance (fF).

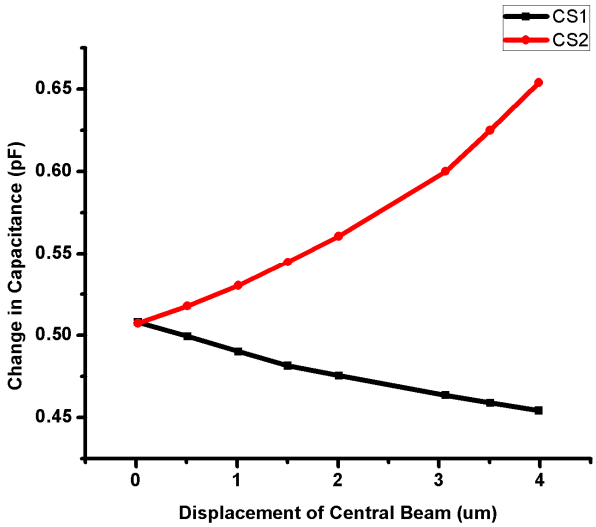

Fig. 15: Graph between displacement at central beam and change in capacitance (fF) obtained by behavioral modeling.

The pull in voltage analysis is carried out to predict the maximum operating voltage of the actuator of the microtweezer. Analytically the maximum pull in voltage calculated through Eq. 8 is 55 V while through system level simulation 58 V is obtained. These results are approximately same.
The above defined parameters are summarized in Table:1, which reveals that the possibility of developing a prosperous device are higher because of the fact that the analytical and behavioral models results are nearly equal.

Parameter	Analytical results	Behavioral model results
Maximum Central Beam moment (μm)	6.3	7.039
Maximum Jaw Displacement (μm)	34.3	38
Capacitance (fF)	C_{s1} 306fF C_{s2} 712fF	C_{s1} 0.45pF C_{s2} 0.65pF
Pull-in voltage (V)	0 - 55	0 - 58

Table 1: Comaprison between analytical and behavioral model results.

8. Conclusions

A MEMS based microtweezer integrated with capacitive touch sensor has been designed using SOI-MUMPS process. The layout model of the device is developed in MEMSPro CAD tool environment. The designed microtweezer gives analytically central beam displacement of 6.3 μm, single jaw displacement of 7.03 μm, capacitance change of C_{S1}=306 *f*F and C_{S2}=712 *f*F and result of pull-in voltage is 55 V.
Extensive simulation through behavioral modeling using the architect module of the CoventorWare verifies the maximum central beam movement of 7.03 μm and jaw displacement of 38 μm with change in capacitance of 0.45*p*F to 0.65*p*F. Pull-in voltage analysis shows that at 58 V, actuator gives maximum performance. The use of analytical and simulation approach avoids iterative fabrication that is expensive. The microtweezer is now ready to send for fabrication with higher chances of its success.

References

[1] N. Dechev, W.L. Cleghorn, and , J.K. Mills, "Microassembly of 3D microstructures using a compliant, passive microgripper", *Journal of Microelectromechanical Systems,* Vol. 13, No. 2, pp. 176-189, 2004.

[2] T. Chen, L. Chen, and L. Sun, "Pizeoelectrically driven silicon microgripper integrated with sidewall piezoresistive sensor", *Proceedings of the IEEE International Conference on Robotics and Automation*, Kobe, Japan, pp. 2989-2994, 2009.

[3] S. Venugopal, L.C. Jsu, S.M.N. Rao, B.P.Wang, M. Chiao, and J.C. Chiao, "Design and modeling of a high accuracy, three degree of freedom MEMS manipulator", *Conference on MEMS and Photonics*, Brisbane, Australia, 2005.

[4] B. R. Jong, D. M. Brouwer, M. J. Boer, H. V. Jansen, H. M. J. Soemers, and G. J. M. Krijnen, "Design and fabrication of a planar three-DOFs MEMS-based manipulator", *Journal of Microelectromechenical System*, Vol. 19, No. 5, pp. 1116-1130, 2010.

[5] C. J. Kim, A. P. Pissano, and R. S. Muller "Silicon-processed overhanging microgripper", *Journal of Microelectromechenical System*, Vol. 1, No. 1, pp. 31–36, 1992.

[6] B. V. Volland, H. Heerlein, and I. W. Rangelow, "Electrostatically driven microgripper", *Journal of Microelectronic Engineering*, Vol. 61 , pp. 1015-1023, 2002.

[7] J. V. Clark, N. Zhou, S. Brown and K. S. J. Pister, "MEMS Simulation Using SUGAR v0.5", *Solid-State Sensors and Actuators* pp. 191-196, 1998.

[8] Q. Jing, T. Mukherjee and G. K. Fedder, "Schematic-Based Lumped Parameterized Behavioral Modeling for Suspended MEMS", *International Conference on Computer Aided Design, San Jose*, CA, Nov. 10-14, 2002.

[9] G. C. Wong, G. K. Tse, Q. Jing, T. Mukherjee, G. K. Fedder, "Accuracy and Composability in NODAS", IEEE Int. Workshop on Behavioral Modeling and Simulation, San Jose, CA, 2003.

[10] G. Uma, M. Umapathy, L. Baby Vidhya, M. Maya, T. Sophia and K. Tamilarasi, "Design and Analysis of Resonant Based Gas Sensor", *Sensors Applications Symposium*, Atlanta,. pp 119-121, 2008.

[11] A. Manut and M. I. Syono "Effects of Mechanical Geometries on resonance Sensitivity of MEMS Out-of-Plane Accelerometer", *IEEE International Conference on Semiconductor Electronics*, Kuala Lumpur, 2006.

[12] Kashif Riaz, Shafaat A. Bazaz, M. Mubasher Saleem and Rana I. Shakoor, "Design, Damping Estimation and Experimental Characterization of Decoupled 3-DoF Robust MEMS Gyroscope", *Journal of Sensors and Actuators A.,* Vol. 172, No. 2, pp. 523-532, 2011.

[13] K. Miller, A. Cowen, G. Hames, B. Hardy, SOIMUMPs Design Handbook, Version 4, MEMSCAP Inc., 2004. Available at: http://www.memscap.com/products/mumps/soimumps/reference-material

[14] Universal Capactive Readout™ IC (MS3110) manual Irvine Sensor Coropration. Available at: http://www.irvine sensors.

[15] M. Bao, "Analysis and design principles of MEMS devices" *1st edition Elsevier*, 2005.

[16] R. Legtenberg, A. W. Groeneveld and M. Elwenspoek, "Comb-drive actuators for large displacements", *Journal of Micromechanics Microengineering*, Vol. 6, No. 3 pp. 320-329, 1996.

[17] CoventorWare ARCHITECT, version 2008, Reference: MEMS and Microsystems System-Level Design Coventor, Inc.

[18] K. Amjad, S. A. Bazaz and Y. Lai, "Design of an electrostatic MEMS microgripper system integrated with force sensor", The *20th IEEE international conference on microelectronics*, Sharjah, 2008, pp 275–278, 2008.

[19] F. Krecinic, T.C. Duc, G.K. Lau and P.M. Sarro "Finite element modeling and experimental characterization of an electro-thermally actuated silicon-polymer microgripper", Journal of micromechanics and Microengineering, Vol. 18, pp., 2008.

[20] E.V. Bordatchev and S.K. Nikumb, "Microgripper: Design, finite element analysis and laser microfabrication", proceeding of the international conference on MEMS, NANO and Smart Systems, Canada, pp. 308-313, 2003.

Chaotic Modeling and Simulation (CMSIM) 2 : 179–186, 2014

Adaptive Control for Synchronization of Li Chaotic Systems with Unknown Parameters

Chunming Xu

School of Mathematics, Yancheng Teachers University, Yancheng 224051,PR China
(E-mail: yctcxcm@gmail.com)

Abstract. In this paper, the problems on chaos control and synchronization of Li chaotic systems with unknown parameters are considered. Firstly, the Li chaotic systems are introduced. Secondly, the adaptive control system with only two state feedbacks for synchronization of the Li chaotic systems is presented and the parameter identification method is also given. Sufficient conditions for the stability of the synchronized errors are provided. Finally, numerical studies are performed to verify the effectiveness of presented schemes.
Keywords: chaos, synchronization, unknown parameters, adaptive controller.

1 Instroduction

Since the synchronization of the coupled chaotic dynamical system with different initial conditions was observed by Pecora and Carroll [1], the idea of synchronization of chaotic systems has gained a lot of attention from various disciplines due to its potential application in many fields such as chemical reactions[2], biological systems[3], and secure communications[4], etc. In the past two decades, a variety of types of synchronization approaches in dynamical systems have been proposed such as adaptive control [5], observer based control [6], variable structure control [7], back stepping control [8], impulsive control [9], nonlinear control [10], and so on.

In practical engineering situations, it is often the case that the parameters of chaotic systems are unknown. Therefore, there is an immense need for algorithms that can effectively synchronize chaotic systems with unknown parameters for theoretical research and practical application.

This paper presents the synchronization between Li systems with unknown parameters accompanied by the presented control system contains only two state feedbacks. Based on the Lyapunov stability theory, we prove that the suggested approach can realize chaos synchronization globally and asymptotically and recognize the unknown parameters as well. Numerical simulations demonstrate the effectiveness of the proposed synchronization methods.

The rest of this paper is organized as follows. The problem formulation and systems description are performed in section 2 and section 3, respectively.

Received: 3 December 2013 / Accepted: 18 April 2014
© 2012 CMSIM
ISSN 2241-0503

Section 4 presents the adaptive control method for the Li systems with unknown parameters. Numerical simulations are performed in section 5 to verify the effectiveness of the presented schemes, and concluding remarks are made in the final section.

2 Synchronization

Consider a class of chaotic system which can be described as

$$\dot{x} = f(x) \tag{1}$$

where $x = x_1, x_2, ..., x_n$ are the state vectors. Take system (1) as the drive system, and the response system is defined as

$$\dot{y} = g(y) + u(t, x, y) \tag{2}$$

where $y = y_1, y_2, ..., y_n$ represent the the state vectors, and $f, g : R^n \to R^n$ are two continuous nonlinear vector functions, $u(t, x, y)$ is an $n-$dimensional control signals.

Let $e(t) = y(t) - x(t)$ is the synchronization error. The control goal is to design the controller $u(t, x, y)$ for the response system (2), such that the error system $e(t)$ can be asymptotically stable at the zero equilibrium. In this sense, that is $\lim_{t\to\infty} e(t) = 0$, which implies that the error dynamic system $e(t)$ between the drive system and the response system is globally asymptotically stable.

3 Systems description

Recently, Li constructed a three-dimensional chaotic system [11], which is described by

$$\begin{cases} \dot{x_1} = a(x_2 - x_1) \\ \dot{x_2} = x_1 x_3 - x_2 \\ \dot{x_3} = b - x_1 x_2 - c x_3 \end{cases} \tag{3}$$

where x_1, x_2, x_3 are state variables, and a, b, c are system parameters. When the system parameters are $a = 5, b = 16, c = 1$, the system (3) demonstrates a chaotic attractor. The three-dimensional view of the chaotic strange attractor and some dynamical behavior in different planes for system (3) are shown in Fig. 1.

4 Synchronization of Li system with unknown parameters

Suppose the master system is defined in (3) which drives the slave system given in the following form

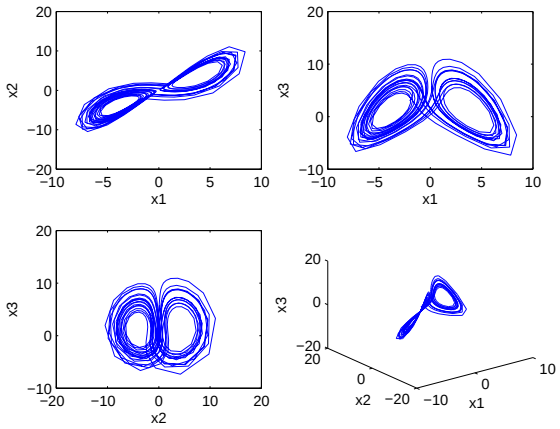

Fig. 1. Typical dynamical behaviors of five-dimensional hyperchaotic Lorenz system.

$$\begin{cases} \dot{y_1} = \widetilde{a}(y_2 - y_1) + u_1 \\ \dot{y_2} = y_1 y_3 - y_2 + u_2 \\ \dot{y_3} = \widetilde{b} - y_1 y_2 - \widetilde{c} y_3 + u_3 \end{cases} \tag{4}$$

where $y_i (i = 1, 2, 3)$ are state variables, $u_i (i = 1, 2, 3)$ are external control inputs, and $\widetilde{a}, \widetilde{b}, \widetilde{c}$ are unknown parameters to be identified.

The error vector can be defined as

$$\begin{cases} e_1 = y_1 - x_1 + u_1 \\ e_2 = y_2 - x_2 + u_2 \\ e_3 = y_3 - x_3 + u_3 \end{cases} \tag{5}$$

So the detail error dynamics is as follows

$$\begin{cases} \dot{e_1}(t) = \widetilde{a}(e_2 - e_1) + \overline{a} x_2 - \overline{a} x_1 + u_1 \\ \dot{e_2}(t) = -e_2 + e_1 e_3 + x_1 e_3 + x_3 e_1 + u_2 \\ \dot{e_3}(t) = \overline{b} - e_1 e_2 - x_1 e_2 - x_2 e_1 - \widetilde{c} e_3 - \overline{c} x_3 + u_3 \end{cases} \tag{6}$$

where $\overline{a} = \widetilde{a} - a$, $\overline{b} = \widetilde{b} - b$ and $\overline{c} = \widetilde{c} - c$.

Theorem. The drive system (3) and the response system (4) can be asymptotically synchronized for any different initial condition with following adaptive controller

$$\begin{cases} u_1 = -\widetilde{a}(e_2 - e_1) - e_1 \\ u_2 = 0 \\ u_3 = e_1 e_2 + x_1 e_2 + x_2 e_1 + (\widetilde{c} - 1) e_3 \end{cases} \tag{7}$$

and the following parameter laws of $\widetilde{a}$,$\widetilde{b}$ and $\widetilde{c}$

$$\begin{cases} \dot{\widetilde{a}} = -x_2 e_1 + x_1 e_1 \\ \dot{\widetilde{b}} = -e_3 \\ \dot{\widetilde{c}} = x_3 e_3 \end{cases} \tag{8}$$

Proof. Firstly, choose Lyapunov function as follows

$$V_1 = \frac{1}{2}(e_1^2 + (\widetilde{a} - a)^2) \tag{9}$$

Its time derivative along the trajectories of (6) is

$$\begin{aligned} &\dot{V_1} = (e_1 \dot{e_1} + \overline{a}\dot{\widetilde{a}}) \\ &= -e_1^2 + e_1(a(e_2 - e_1) + \overline{a}(e_2 - e_1) + e_1 + \overline{a}x_2 - \overline{a}x_1 + u_1) + \overline{a}\dot{\widetilde{a}} \end{aligned} \tag{10}$$

Substituting (7) and (8) into (10), we have

$$\dot{V_1} = -e_1^2 \leq -2V_1(t) \tag{11}$$

which leads to $V_1(t) \leq V_1(0)\exp(-t)$, thus we have $\lim\limits_{t\to\infty} e_1(t) = 0$.

On the other hand, we take another Lyapunov function as

$$V_2 = \frac{1}{2}(e_3^2 + (\widetilde{b} - b)^2 + (\widetilde{c} - c)^2) \tag{12}$$

Its time derivative along the trajectories of (6) is

$$\begin{aligned} &\dot{V_2} = (e_3 \dot{e_3} + \overline{b}\dot{\widetilde{b}} + \overline{c}\dot{\widetilde{c}}) \\ &= -e_3^2 + e_3(\overline{b} - e_1 e_2 - x_1 e_2 - x_2 e_1 - \overline{c}e_3 - \overline{c}x_3 + (1 - c)e_3 + u_3) + \overline{b}\dot{\widetilde{b}} + \overline{c}\dot{\widetilde{c}} \end{aligned} \tag{13}$$

Substituting (7) and (8) into (13), we haven

$$\dot{V_2} = -e_3^2 \leq -2V_2(t) \tag{14}$$

which leads to $V_2(t) \leq V_2(0)\exp(-t)$, thus we have $\lim\limits_{t\to\infty} e_3(t) = 0$.

Now, by solving the second equation of (6) we get the following result

$$e_2 = \exp(-t)(e_2(0)) + \int_0^t \exp(t)(e_1 e_3 + x_1 e_3 + x_3 e_1)dt \tag{15}$$

Because $\lim\limits_{t\to\infty}(e_1 e_3 + x_1 e_3 + x_3 e_1) = 0$, thus by basic calculation one can yield $\lim\limits_{t\to\infty} e_2(t) = 0$. Therefore, the error $e_i(t) = 0 (i = 1, 2, 3)$ will converge to zero.

Consider the first and the third equation of (6) we get the following result

$$\begin{cases} \lim\limits_{t\to\infty} \overline{a}(x_2 - x_1) = 0 \\ \lim\limits_{t\to\infty} \overline{b} = 0 \\ \lim\limits_{t\to\infty} \overline{c}x_3 = 0 \end{cases} \tag{16}$$

then we can have

$$\begin{cases} \lim\limits_{t\to\infty} \widetilde{a} = a \\ \lim\limits_{t\to\infty} \widetilde{b} = b \\ \lim\limits_{t\to\infty} \widetilde{c} = c \end{cases} \tag{17}$$

This completes the proof.

5 Simulation examples

In this section, some numerical simulations about the synchronization between the drive system (3) and the response system (4) are given to verify the effectiveness of the proposed method. In the numerical simulations, the fourth-order Runge-Kutta method is used to solve the system. The system parameters are selected as $a = 5, b = 16, c = 1$ and $a_1 = 4, b_1 = -3, c_1 = 9$, such that the drive system and the response system are chaotic with no control applied. We employed the initial conditions be $x(0) = (2, -4, 6)$ for the drive system and $y(0) = (-1, 1, 2)$ for the response system, respectively.

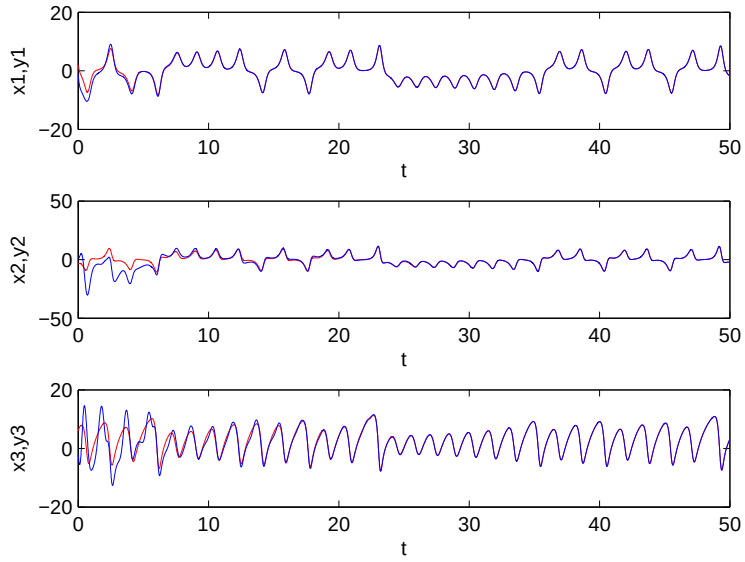

Fig. 2. State trajectories of synchronization between the drive system and the response system.

Numerical results are displayed in Figures 2-4. Fig.2 shows shows the time evolution curves of the drive system and the response system with controllers (7) and parameter laws (8). Fig.3 shows the time evolution of the synchronization errors, which displays that the errors tend to zero as $t \to \infty$. In addition,

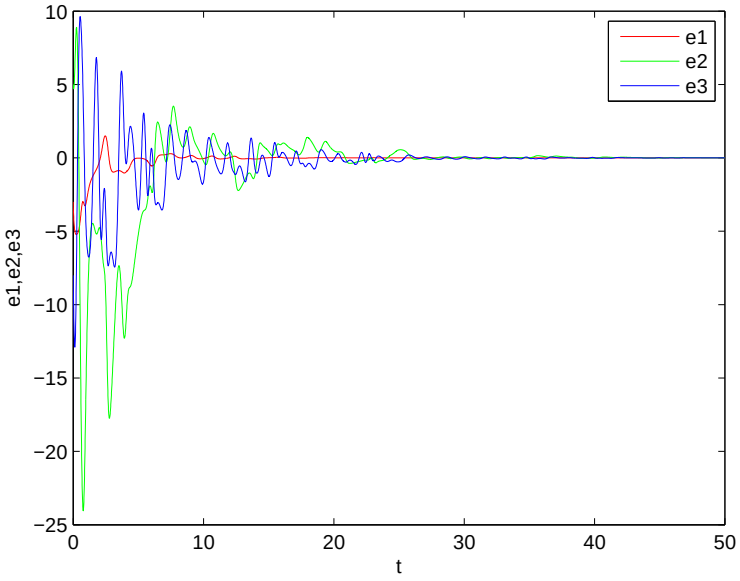

Fig. 3. Time response of the synchronization errors.

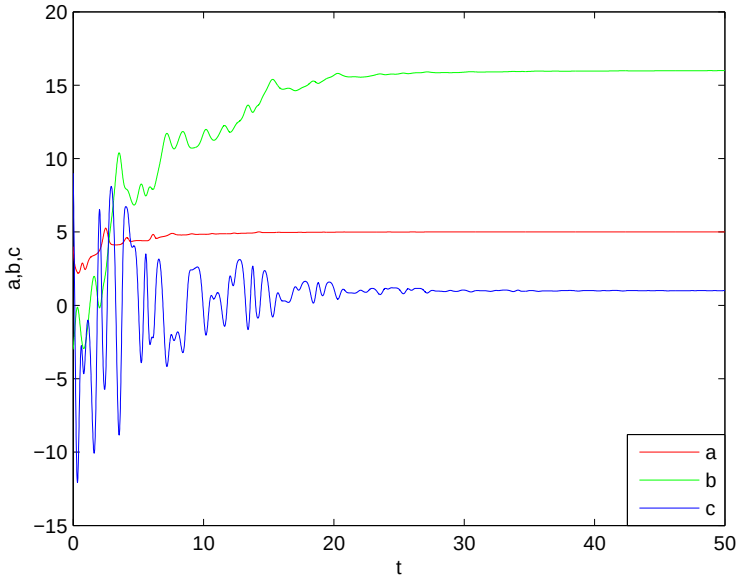

Fig. 4. Graph of the estimate parameters results.

the estimations of the parameters are shown in Fig.4. These results show that synchronization between Li chaotic systems with unknown parameters has been achieved with our designed adaptive controller and parameter laws.

6 Conclusions

In this paper, we have studied the robust adaptive synchronization between two Li chaotic systems with unknown parameters based on adaptive control and stability theory. The effectiveness of the proposed approach has been verified by the numerical simulations. The proposed adaptive control method can not only achieve synchronization but also identify the system parameters at the same time. The presented control method can also be applied in many other chaotic systems.

Acknowledgements

This work is partially supported by the National Natural Science Foundation of China (No. 61273106 and No.11301457) and the Natural Science Foundation of the Jiangsu Higher Education Institutions of China (No.12KJD110007 and No.13KJD520010).

Bibliography

[1] L.M. Pecora, T.L. Carroll:" Synchronization in chaotic systems"; Phys. Rev. Lett.,Vol. 64(8), 1990, 821-824

[2] Y.N. Li, L. Chen, Z.S. Cai, X.Z. Zhao: " Experimental study of chaos synchronization in the Belousov-Zhabotinsky chemical system"; Chaos Solitons Fractals, Vol. 22(4), 2004, 767-771.

[3] R.A. Ims, H.P. Andreassen: " Spatial synchronization of vole population dynamics by predatory birds" ; Nature, Vol. 408(9), 2000, 194-196.

[4] L. Kacarev, U. Parlitz: " General approach for chaotic synchronization, with application to communication"; Phys. Rev. Lett., Vol. 74(25), 1996, 5028-5031.

[5] M.T. Yassen: "Adaptive control and synchronization of a modified Chuas system"; Appl. Math. Comput. , Vol. 135(1), 2003, 113-128.

[6] M. Chen, W. Min: " Unknown input observer based chaotic secure communication"; Phys. Lett. A , Vol. 372(10), 2008, 1595-1600.

[7] Utkin VI: "Variable structure systems with sliding modes"; IEEE Trans Automat Contr, Vol. 22(2), 1977, 212-222

[8] Huang L, Wang M, Feng R: "Synchronization of generalized Henon map via backstepping design"; Chaos, Solitons and Fractals, Vol. 23(2), 2005, 617-620.

[9] T.Wang, X.Wang, and M.Wang: " A simple criterion for impulsive chaotic synchronization"; Communications in Nonlinear Science and Numerical Simulation, Vol. 16(3), 2011, 1464-1468, 2011.

[10] Chen H:" Global chaos synchronization of new chaotic systems via nonlinear control"; Chaos, Solitons and Fractals , Vol. 23(4), 2005, 1245-1251.

[11] X.F. Li, K.E. Chlouverakis, D.L. Xu: " Nonlinear dynamics and circuit realization of a new chaotic flow: a variant of Lorenz, Chen and Lü "; Nonlinear Analysis, Vol. 10(4), 2009, 2357-2368.

Chaotic Modeling and Simulation (CMSIM) 2: 187–192, 2014

On a Topological Problem of Strange Attractors

Ibrahim Kirat[1] and Ayhan Yurdaer[2]

[1] Department of Mathematics, Istanbul Technical University, 34469 Maslak, Istanbul, Turkey
(E-mail: ibkst@yahoo.com)
[2] Department of Mathematics, Istanbul Technical University, 34469 Maslak, Istanbul, Turkey
(E-mail: yurdaerayhan@itu.edu.tr)

Abstract. In this note, we consider self-affine attractors that are generated by an expanding $n \times n$ matrix (i.e. all of its eigenvalues have moduli > 1) and a finite set of vectors in $\mathbb{Z}^n$. Here we concentrate on the problem of connectedness. Although, there has been intensive study on the topic recently, this problem is not settled even in the one-dimensional case. We focus on some basic attractors, which have not been studied fully, and characterize connectedness.
Keywords: Self-affine attractors, Self-affine tiles, Connectedness.

1 Introduction

Let $S_1, ..., S_q$, $q > 1$, be contractions on $\mathbb{R}^n$, i.e., $||S_j(x) - S_j(y)|| \leq c_j||x - y||$ for all $x, y \in \mathbb{R}^n$ with $0 < c_j < 1$. Here $|| \cdot ||$ stands for the usual Euclidean norm, but this norm may be replaced by any other norm on $\mathbb{R}^n$. It is well known [4] that there exists a unique non-empty compact set $F \subset \mathbb{R}^n$ such that

$$F = \bigcup_{j=1}^{q} S_j(F).$$

Let $M_n(\mathbb{R})$ denote the set of $n \times n$ matrices with real entries. We will assume that

$$S_j(x) = T^{-1}(x + d_j), \qquad x \in \mathbb{R}^n,$$

where $d_j \in \mathbb{R}^n$, called *digits*, and $T \in M_n(\mathbb{R})$. Then F is called a *self-affine set* or a *self-affine fractal*, and can be viewed as the invariant set or the attractor of the (affine) *iterated function system* (IFS) $\{S_j(x)\}$ (in the terminology of dynamical systems). Let $M_n(\mathbb{Z})$ be the set of $n \times n$ integer matrices. Further, if $D := \{d_1, ..., d_q\} \subset \mathbb{Z}^n$ and $T \in M_n(\mathbb{Z})$, it is called an *integral self-affine set* and we will primarily consider such sets in this paper. If, additionally, $|\det(T)| = q$ and the integral self-affine set F has positive Lebesgue measure, then F is called an *integral self-affine tile*. We sometimes write $F(T, D)$ for

Received: 7 August 2013 / Accepted: 5 April 2014
© 2014 CMSIM
ISSN 2241-0503

F to stress the dependence on T and D. For such tiles, the positivity of the Lebesgue measure is equivalent to having nonempty interior [2].

There is a demand to develop analysis on fractal spaces, in order to deal with physical phenomena like heat and electricity flow in disordered media, vibrations of fractal materials and turbulence in fluids. Without a better understanding of the topology of fractals, this seems to be a difficult task. There is a growing literature on the formalization and representation of topological questions; see [3] for a survey of the field.

One of the interesting aspects of the self-affine sets is the *connectedness*, which roughly means the attractor cannot be written as a disjoint union of two pieces. This property is important in computer vision and remote sensing [8,20]. We mention that connected self-affine fractals are curves; thus, they are sometimes referred to as self-affine curves [10]. There is some motivation for studying connected self-affine tiles because they are related to number systems, wavelets, torus maps. Recently, there have been intensive investigations on the topic by Kirat and Lau [12,10], Akiyama and Thuswaldner [1,16], Ngai and Tang [18,19] and Luo et al. [16,15].

In this note, we consider planar integral self-affine fractals obtained from 2×2 integer matrices with reducible characteristic polynomials, and report our findings on their connectedness. However, our considerations can be generalized to higher dimensions. As for the organization of the paper, in Section 2, we deal with special cases and state some simple, but unconventional techniques to check the connectedness. In literature, most of the papers on the connectedness have some restrictions on the digit set. Here our aim is to remove such restrictions in Section 3.

2 Some Unconventional Techniques

Usually, connectedness criteria were given by using a "graph" with vertices in D [6,12]. In this section, we present graph-independent techniques to check the connectedness or disconnectedness. Throughout the paper, T^{-1} is a contraction. Let $\#D$ denote the number of elements in D. We first recall a known result.

Proposition 1. *[12] Suppose $T=[\pm q]$ with $q\in\mathbb{N}$, and $D\subseteq\mathbb{R}$ with $\#D=q$. Then $F(T,D)$ is a connected tile if and only if, up to a translation, $D=\{0,a,2a,...,(q-1)a\}$ for some $a>0$.*

As one may notice q and D are not arbitrary in Proposition 1 since $q\in\mathbb{N}$ and $\#D=q$. By using the approach in [9,11], we can remove such restrictions. For that purpose, we consider the convex hull of F and denote it by K. Also let $K_1=\bigcup_{j=1}^{q} S_j(K)$. Then we have the following.

Proposition 2. *Let $D=\{0,d_2v,\cdots,d_qv\}\subset\mathbb{R}^n$ with $v\in\mathbb{R}^n\setminus\{0\}$ and $T=pI$, where $p\in\mathbb{R}$ and I is the identity matrix. Then $F(T,D)$ is connected if and only if $K=K_1$.*

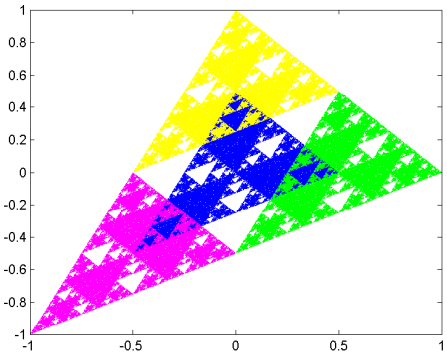

Fig. 1. The Sierpiński tile

Remark 1. A digit set D as in Proposition 2 is called a *collinear* digit set. It is easy to check the condition $K = K_1$ in the proposition because K is a closed interval. If $T = \pm 2I$, then $F(T, D)$ is connected for any digit set. A famous example of this type is the Sierpiński tile (see Figure 1), for which $T = 2I$ and $D = \{d_1 = \left[\begin{smallmatrix} 0 \\ 0 \end{smallmatrix}\right], d_2 = \left[\begin{smallmatrix} 1 \\ 0 \end{smallmatrix}\right], d_3 = \left[\begin{smallmatrix} 0 \\ 1 \end{smallmatrix}\right], d_4 = \left[\begin{smallmatrix} -1 \\ -1 \end{smallmatrix}\right]\}$.

The disconnectedness of $F(T, D)$ was studied in [13]. Here we want to mention another unconventional sufficient condition for disconnectedness. In the rest of the paper, we study attractors $F(T, D)$ in the plane such that $T \in M_2(\mathbb{Z})$ has a reducible characteristic polynomial. From [10], we know that such matrices are conjugate to one of the following lower triangular matrices

$$\begin{bmatrix} n & 0 \\ t & m \end{bmatrix}, \quad \text{where } |n| \geq |m|, \text{ and } t = 0 \text{ or } t = 1. \tag{1}$$

We also let

$$S = \{\left[\begin{smallmatrix} i \\ j \end{smallmatrix}\right] : 0 \leq i \leq |n| - 1,\ 0 \leq j \leq |m| - 1\}.$$

The attractors of the next proposition can be considered as a generalization of Sierpiński carpets [17]. Let $dim_S(F)$ be the *singular value dimension* of F (see [5]). We call a collinear digit set D with v is an eigenvector of T *eigen-collinear*. In that case, F is a subset of a line segment. By using Corollary 5 in [5], we obtain the following.

Proposition 3. *Assume that T is as in (1), $D \subset S$, and D is not eigen-collinear. Then $F(T, D)$ is disconnected if $\log_{|m|} r + \log_{|n|}(\frac{q}{r}) \neq dim_S(F)$, where $q = \#D$ and r is the number of j so that $\left[\begin{smallmatrix} i \\ j \end{smallmatrix}\right]$ for some i.*

Remark 2. It is easy to check the sufficient condition for the attractors $F(T, D)$ in Proposition 3 because, in that case,

$$dim_S(F) = \begin{cases} 1 + \log_{|n|}(\frac{q}{|m|}) & \text{if } |m| < q \leq |mn|, \\ \log_{|m|} q & \text{if } q \leq |m|. \end{cases}$$

3 General Digit Sets

In this section, we will present a practical way of checking the connectedness of $F(T,D)$ with T as in (1) and $D \subset \mathbb{Z}^2$. Note that it is enough to consider the case $n,m>0$, since $F(T,D)=F(T^2,D+TD)$. By translating D, we will assume that D has nonnegative entries. Let $\mathcal{N}=(F-F)\cap\mathbb{Z}^2$. Set

$$\Delta D = D-D, \quad a_1=\begin{bmatrix} n-1 \\ 1 \end{bmatrix}, \quad a_2=\begin{bmatrix} 0 \\ m-1 \end{bmatrix}, \quad a_3=\begin{bmatrix} n-1 \\ m-1 \end{bmatrix}, \quad b_1=\begin{bmatrix} n-1 \\ 0 \end{bmatrix},$$

$$e_1=\begin{bmatrix} 1 \\ 0 \end{bmatrix}, \ e_2=\begin{bmatrix} 0 \\ 1 \end{bmatrix}, \ e_3=\begin{bmatrix} 1 \\ 1 \end{bmatrix}, \ e_4=\begin{bmatrix} 1 \\ -1 \end{bmatrix}.$$

First, we begin with the special class of fractals F in Proposition 3, where $D \subset S$.

Proposition 4. *Assume that F is as in Proposition 3, $t=1$ and $n,m>0$. Then*

(i) if $a_2 \notin \Delta D$, then F is disconnected,

(ii) otherwise,

$\mathcal{N}=\{\pm e_i \mid i\in\{1,2\} \text{ and } a_i \in \Delta D\}\cup\{\pm e_4 \mid \ a_1-a_2\in\Delta D\}$.

Proposition 5. *Assume that F is as in Proposition 3, $t=0$ and $n,m>0$. Let $b_2=a_2$, $b_3=a_3$. Then*

(i) if $b_1,b_2,b_3,b_1-b_2\notin\Delta D$, then F is disconnected,

(ii) otherwise,

$\mathcal{N}=\{\pm e_i \mid i\in\{1,2,3\} \text{ and } b_i \in \Delta D\}\cup\{\pm e_4 \mid \ b_1-b_2\in\Delta D\}$.

For a digit set D, an *s-chain* (in D) is a finite sequence $\{d_1,...,d_s\}$ of s vectors in D such that $d_i-d_{i+1}\in\mathcal{N}$ for $i=1,...,s-1$. Then we can put the connectedness criterion in [12] into the following form.

Proposition 6. *F is connected if and only if, by re-indexing D (if necessary), D forms a q-chain.*

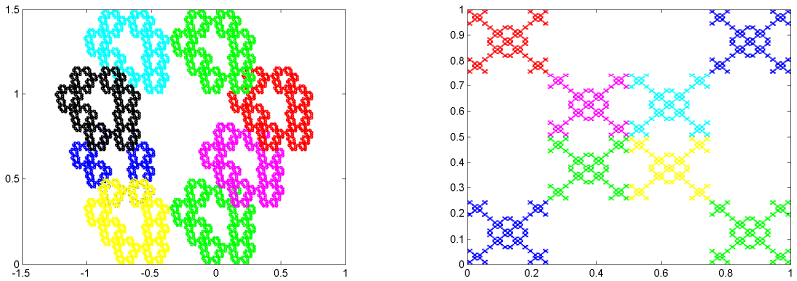

Fig. 2.

Remark 3. Note that if $D = \{d_1, ..., d_q\}$ after re-indexing, it is possible that $d_i = d_j$ for $i \neq j$. In view of Proposition 4 and Proposition 5, Proposition 6 is quite feasible. That is, the connectedness can be decided by a simple inspection of D using $\mathcal{N}$ in Propositions 4-5. That is, we get a graph-independent way of checking the connectedness. Two examples are given in Figure 2, for which $T = \left[\begin{smallmatrix} -3 & -1 \\ 0 & 3 \end{smallmatrix}\right]$, and $D = \{d_1 = \left[\begin{smallmatrix} 0 \\ 0 \end{smallmatrix}\right], d_2 = \left[\begin{smallmatrix} 2 \\ 1 \end{smallmatrix}\right], d_3 = \left[\begin{smallmatrix} -1 \\ 1 \end{smallmatrix}\right], d_4 = \left[\begin{smallmatrix} 1 \\ 3 \end{smallmatrix}\right], d_5 = \left[\begin{smallmatrix} 2 \\ 0 \end{smallmatrix}\right], d_6 = \left[\begin{smallmatrix} 2 \\ 2 \end{smallmatrix}\right], d_7 = \left[\begin{smallmatrix} -2 \\ 2 \end{smallmatrix}\right], d_8 = \left[\begin{smallmatrix} -1 \\ 3 \end{smallmatrix}\right]\}$, and for the second fractal on the right $T = 4I$ and $D = \{d_1 = \left[\begin{smallmatrix} 0 \\ 0 \end{smallmatrix}\right], d_2 = \left[\begin{smallmatrix} 1 \\ 1 \end{smallmatrix}\right], d_3 = \left[\begin{smallmatrix} 2 \\ 2 \end{smallmatrix}\right], d_4 = \left[\begin{smallmatrix} 3 \\ 3 \end{smallmatrix}\right], d_5 = \left[\begin{smallmatrix} 2 \\ 1 \end{smallmatrix}\right], d_6 = \left[\begin{smallmatrix} 1 \\ 2 \end{smallmatrix}\right], d_7 = \left[\begin{smallmatrix} 0 \\ 3 \end{smallmatrix}\right], d_8 = \left[\begin{smallmatrix} 3 \\ 0 \end{smallmatrix}\right]\}$.

We now consider the general case $D \subset \mathbb{Z}^2$. Let

$$\mathcal{M}_1 = \{\pm(ke_1 \pm le_2) \mid \ k, l \in \mathbb{N} \text{ and } ka_1 \pm la_2 \in \Delta D\},$$

$$\mathcal{M}_0 = \{\pm(ke_1 \pm le_2) \mid \ k, l \in \mathbb{N} \text{ and } kb_1 \pm lb_2 \in \Delta D\}.$$

Note that it is possible that $\mathcal{M}_1 = \emptyset$ or $\mathcal{M}_0 = \emptyset$.

Proposition 7. *Assume that T is as in (1) with $t = 1$, $n, m > 0$ and $D \subset \mathbb{Z}^2$. Then*

(i) if $ka_2, ka_1 \pm la_2 \notin \Delta D$ for all $k, l \in \mathbb{N}$, then F is disconnected,

(ii) otherwise, then $\mathcal{N} = \{\pm ke_i \mid k \in \mathbb{N},\ i \in \{1, 2\}$ and $ka_i \in \Delta D\} \cup \mathcal{M}_1$.

Proposition 8. *Assume that T is as in (1) with $t = 0$, $n, m > 0$ and $D \subset \mathbb{Z}^2$. Let $b_2 = a_2$, $b_3 = a_3$. Then*

(i) if $kb_1, kb_2, kb_3, kb_1 \pm lb_2 \notin \Delta D$ for all $k, l \in \mathbb{N}$, then F is disconnected,

(ii) otherwise, then $\mathcal{N} = \{\pm ke_i \mid k \in \mathbb{N},\ i \in \{1, 2, 3\}$ and $kb_i \in \Delta D\} \cup \mathcal{M}_0$.

References

1.S. Akiyama and J. M. Thuswaldner, *Topological properties of two-dimensional number systems*, J. Theor. Nombres Bordeaux, **12** (2000), 69-79.

2.C. Bandt, Self-similar sets 5. Integer matrices and fractal tilings of $\mathbb{R}^n$, Proc. Amer. Math. Soc. 112 (1991) 549-562.

3.T. K. Dey, H. Edelsbrunner, and S. Guha, *Computational topology* in Advances In Discrete and Computational Geometry, B. Chazelle, J. E. Goodman and R. Pollack, eds., Contemp. Math., Vol 223, American Mathematical Society, Providence, RI, 1999, pp. 109-143.

4.K.J. Falconer, Fractal geometry: Mathematical Foundations and Applications, John Wiley & Sons, Chichester, 1990.

5.K. J. Falconer, The dimension of self-affine fractals II, Math. Proc. Cambridge Philos. Soc. 111 (1992) 169-179.

6.M. Hata, *On the structure of self-similar sets*, Japan J. Appl. Math., **2** (1985), no. 2, pp. 381-414.

7.X.-G. He, K.-S. Lau, and H. Rao, Self-affine sets and graph-directed systems, Constr. Approx., 19 No.3, (2003) 373-397.

8.G.T. Herman, and E. Zhao, *Jordan surfaces in simply connected digital spaces*, J. Math. Imaging Visison, **6** (2003), 121-138.

9.I. Kirat, Boundary Points of Self-Affine Sets in R, Turk. J. Math., 27 (2003), no 2, 273-281.

10.I. Kirat, Disk-like tiles and self-affine curves with non-collinear digits, Math. Comp., 79 no.6 (2010) 1019-1045.
11.I. Kirat and I. Kocyigit, Remarks on self-affine fractals with polytope convex hulls, Fractals **18** no.4 (2010) 483-498.
12.I. Kirat and K.S. Lau, On the connectedness of self-affine tiles, J. London Math. Soc. 2, 62 (2000), 291-304.
13.I. Kocyigit, "Disconnectedness of self-affine sets and a method for finding the convex hulls of self-affine sets", M. Sc. Thesis, Istanbul Technical University, (2007).
14.J. Luo, *Boundary local connectivity of tiles in* $\mathbb{R}^2$., Topology Appl., **154** (2007), no. 3, 614-618.
15.J. Luo, H. Rao and B. Tan, *Topological structure of self-similar sets*, Fractals, **10** (2002), 223-227.
16.J. Luo and S. Akiyama and J. M. Thuswaldner, *On the boundary connectedness of connected tiles*, Math. Proc. Cambridge Philos. Soc., **137** (2004), no. 2, 397-410.
17.C. McMullen, The Hausdorff dimension of general Sierpiński carpets, Nagoya Math. J. 96 (1984) 1-9.
18.S. M. Ngai and T. M. Tang. *A technique in the topology of connected self-similar tiles*, Fractals, **12** (2004), no.4, 389-403.
19.S. M. Ngai and T. M. Tang. *Topology of connected self-similar tiles in the plane with disconnected interiors.* , Topology Appl., **150** (2005), no.1-3, 139-155.
20.A. Rosenfeld, *Connectivity in digital pictures*, J. ACM, **17** (1970), 146-160.

Chaotic Modeling and Simulation (CMSIM) 2: 193–198, 2014

The profile of temperature in the dissipative over-dense plasma layer

L. Rajaei[1⋆] , S. Miraboutalebi[2]

[1] Physics Department, Qom University, Qom, Iran
(E-mail: rajaeel@yahoo.com)
[2] Physics Department, Islamic Azad University, North Tehran Branch, Tehran, 1651153311, Iran
(E-mail: smirabotalebi@gmail.com)
[1]

Abstract. An investigation is undertaken to introduce an effective mechanism of plasma heating which significantly enhances and facilitates the heating of a dense plasma layer. This mechanism directly related to the phenomena of anomalous transparency of a dense plasma layer through the resonant excitation of the coupled surface waves. It is shown that the collisional effects reduce the rate of the energy transmission through the plasma layer under resonant conditions. This dissipative effects cause heating of the plasma layer to a considerable amount of temperature. The temperature distribution in the plasma layer during the transmission of the electromagnetic waves is studied.
Keywords: Microwave, Dissipation, Incident wave, Over-dense plasma, Surface plasma, Transparency.

1 Introduction

The investigations of circumstances and important factors in the plasma heating is the subject of relevance for many fields of plasma physics ranging from laboratory experiments to astrophysics [1]. The heat flow and temperature gradient in plasma are fundamental process that take place during plasma phenomenons and are of grate importance effects. These process in some situations, have inevitable destructive effects. One of the challenges of embedding plasma in electric field is the appearance of high temperature electrons which acts like an internal transport barrier. The three well known heating mechanisms of plasma are ohmic heating, neutral beam injection and high frequency electromagnetic waves. In the high frequency electromagnetic waves mechanism of plasma heating, the energy of waves is converted into thermal electron motion through electron-ion collisions [2,3]. Also the interaction of the electromagnetic waves with plasma may lead to the resonant excitation of the electrostatic waves which subsequently decays generating energetic electrons [4].

⋆ Corresponding author: Tel +98-25-32854972. E-mail address: rajaeel@yahoo.com

[1] Received: 7 August 2013 / Accepted: 10 April 2014
© 2014 CMSIM
ISSN 2241-0503

In our previous works we studied the total transparency conditions of an overdense plasma layer due to the resonant excitation of the coupled surface modes, [5]-[9]. In the present paper we demonstrate another mechanism of plasma heating that significantly enhances and facilitates the heating of the dense plasma. We will show that for a collisional plasma under resonant conditions, the dissipative effects cause heating of the dense plasma to a considerable amount of temperature. Hence the process of resonant excitation of the coupled plasmons can be considered as an effective mechanism of plasma heating. In fact this process has a dual acting effect, it cause the transparency of the plasma slab and at the same time it gives rise to plasma heating.

This paper is organized as follows: In section two the geometrical construction of the problem and the transmission of the electromagnetic waves through the considered structure. In section three the solutions of the heat equations at steady states condition is given and the temperature is predicted. Finally, section four presents the results.

2 the model

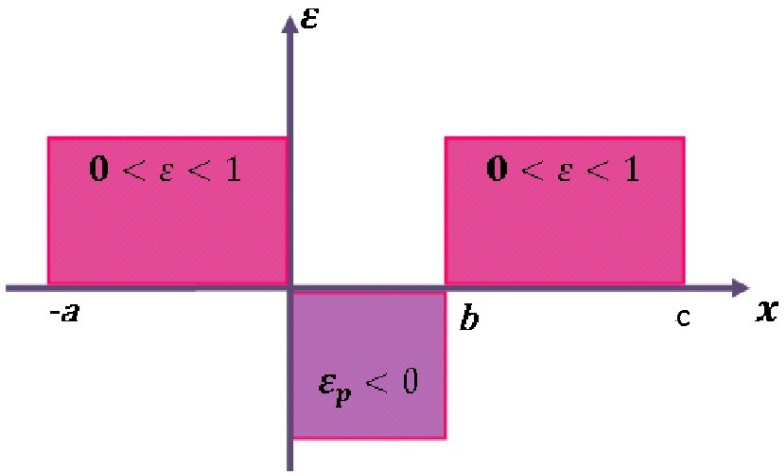

Fig. 1. Schematic diagram showing the spatial distribution of the effective electric permittivity.

Let us consider a geometrical structure fulfills the conditions under which the high transparency of a normally reflected overdense plasma can be observed , [7]. The system is modeled as an overdense plasma layer with length b placed between two equal ordinary dielectrics or equivalently cold plasma layer (see Fig. 1). In order to examine the resonant conditions of the excitation of the surface modes let us consider a p-polarize wave specified by the magnetic field component $\mathbf{B} = (0, 0, B_z)$ and the electric field in the plane of incidence (x, y),

namely $\mathbf{E} = (E_x, E_y, 0)$. Considering the geometrical structure of Fig. (1), the spatial part of the electric and the magnetic fields must be proportional to $exp(iky)$ and the waves amplitudes become functions only of the variable x. In this case the magnetic field and temperature at the steady state, obtain the following forms:

$$\kappa \frac{\partial^2 T}{\partial^2 x} + Q = 0. \tag{1}$$

$$\epsilon \frac{\partial}{\partial x} \frac{1}{\epsilon} \frac{\partial B_z}{\partial x} + (\epsilon - k_y^2) B_z = 0\,. \tag{2}$$

where κ refers to the thermal conductivity. Also,

$$Q = \frac{\epsilon_0}{2} \epsilon'' \omega E_0^2 |\mathbf{E}|\,, \tag{3}$$

where ϵ'' is the imaginary part of the permittivity. Here $\epsilon = (1 - \frac{\omega_p^2}{\omega^2 s})$, $s = (1 + i\nu/\omega)$, also $k_0 = \frac{\omega}{c}$ and $\omega_p = \frac{4\pi n_0 e^2}{m}$. In these equations, all field quantities have become dimensionless and redefined as follows:

$$\left(\tilde{\mathbf{r}} = k_0 \mathbf{r}\,,\, \tilde{t} = \omega t\right)\,,\, \tilde{\mathbf{E}} = \frac{\mathbf{E}}{E_0}\,,\, \tilde{\nu} = \frac{\nu}{\omega}\,,\, \tilde{T} = \frac{T}{T_0}\,, \tag{4}$$

where the tilde quantities are dimensionless, but for simplicity, we ignore the tilde sign of our field quantities in equations. Likewise, the temperature should satisfy the surface heat balances. where $k_y = sin\theta$. Analytical solutions of Eqs.(2)gives the magnetic field in the both dielectrics and the over dense plasma mediums, and are obtained in the following forms:

$$B_z = (A_1 e^{\alpha x} + A_2 e^{-\alpha x}), \tag{5}$$

where $\alpha = \sqrt{k_y^2 - \epsilon}$. The electromagnetic fields in the vacuum regions, $x < -a$ and $x > b$, have the following forms:

$$B_z = E_0 e^{\imath \cos\theta x} + R e^{-\imath \cos\theta x} \quad x < -a\,, \tag{6}$$

$$B_z = T_r e^{\imath \cos\theta x} \quad x > b\,, \tag{7}$$

where E_0, R and T respectively assign the field components for the incident, reflected and transmitted waves.

These field solutions should satisfy the conditions of continuity of dB_z/dx and B_z, on all the boundaries and as a result, one achieve eight equations for the unknown coefficients, specifically the coefficient R and T_r are obtained. For resonant values of the incident angle θ, we should expect anomalous transmission of the electromagnetic waves.

Fig. (2) shows the transmission curve T_r and R as a function of the incidence angle θ for two different values of the collisional frequencies, namely for $\nu = 0.1$ and $\nu = 0.2$. Two important results are obtained from these plots. As the first

result, there is an acute increase in the transmission properties of the system, when the angle of incidence reaches to one of its resonant values. According to the figure.(2), the maximum of the transmission coefficient T occurs about $\theta = 0.18rad$ for two different value of collisional frequencies.

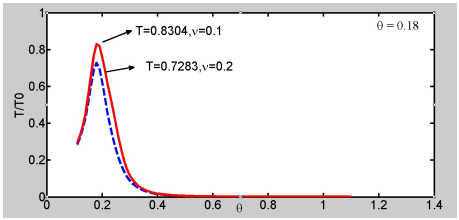

Fig. 2. The transmission coefficients vs incident angel for two different value of collisional frequency

As the second result, comparing the two maximums indicates that, with the increase of the collisional frequency ν, t he maximum rate of the electromagnetic waves decreases. In order to investigate the effect of this dissipated energy on the increase of the plasma temperature, the electric field amplitude in the over-dense plasma at the maximum points is needed. To provide this we note that for the case $\nu = 0.1$, the deficiency at the maximum point is about $1 - (\mid R \mid^2 + \mid T_r \mid^2) = 0.3071$, while For the case $\nu = 0.2$ the deficiency is about $1 - (R^2 + T_r^2) = 0.4373$.

3 The heat equation

In order to investigate the temperature variations or the increase of the temperature degree of the over-dense plasma due to passing of the electromagnetic waves one should consider the solutions of the heat equation (1). The factor Q that is given in Eq.(3) can be considered as a thermal source for the heat equation. The imaginary part of the permittivity explicitly appears in the heat source and hence is vitally important to produce heat. Also the heat source Q depends on the amplitude of the passing electric field in the over-dense plasma layer. The electric field amplitudes, obtained in previous section, in the over-dense plasma layer under the resonant transmission of waves. Substituting them in Eq. (3) for each value of the collisional frequency ν, the heating source Q would be obtained. Subsequently one can study the temperature variations and the key factors of these variations by solving the corresponding heat equation via Eq.(1).

Here we follow the above procedure and analyze the temperature variations from Eq.1 in steady state both numerically and analytically.

we require only the boundary condition which includes convection relation on both boundaries of the plasma.

$$T(x) = 1, x = 0, \quad \frac{\partial T}{\partial x} = 0, x = b.$$

It should be noticed that the sample or the plasma will be kept in room temperature, therefore, T_0 is the room temperature also here T is dimensionless and equals to T/T_0 . Heat equation will be solved through analytic as well as the numerical method and, subsequently, compare the data obtained. The analytical answers of this equation are as follows:

$$T(x) = -\frac{1}{\kappa}\int\int Q(x)dxdx + C_1 x + C_2, \tag{8}$$

where C_1 and C_2 are calculated by boundary conditions.Also Eq. 8 can be written in the following form

$$T(x) = -F_1(x) + F_2(0)x + F_1(0), \tag{9}$$

where $F_1(x) = \int\int Q(x)dx, F_2(x) = \int Q(x)dx$,

The above relation demonstrates that the curve of temperature is an ascending function of space. To investigate this more closely, the analytical solutions of the temperature functions obtained from Eq.1 are plotted in Fig. (3a).This figure contains two different curves corresponding to two different values of the collisional frequencies ν. As it is shown in the figure, the plasma temperature increases as one move away from the plasma fronting edge. It should be noticed that this temperature rising takes place due to the collisional effects which appears in the form of the thermal source term Q.

It is also plotted the temperature curve by using a numerical method and the results are given in Fig. (3b). To solve the heat equation (1) numerically, the finite difference method has been employed. These numerical results are in a good agreement with the analytical results and show an ascending function of space for the temperature function.

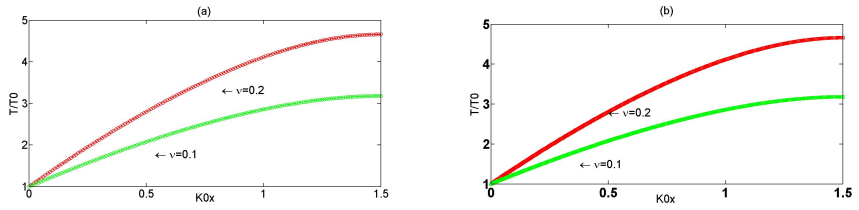

Fig. 3. The profile of temperature for analytic and numeric solutions.

4 Conclusions

It has been shown here that the coupled resonant excitation of the surface modes could create a condition for suitably heating of a dense collisional plasma layer. To provide the resonant conditions, the plasma layer was considered between two dielectric layers. The slab then was supposed to be subjected to the electromagnetic waves. After solving the equation of the wave for a cold

plasma, the electric field in all mediums was obtained. Eventually, the energy transmission on the rear side of the dielectric layer was examined. Here, the important issue is the effect of the collision on the amount of energy transmission which, as researchers have shown, diminishes as the collisional effects increase. Equally the important issue is the way in which the dissipative energy in the plasma appears. The results indicate that the dissipated energy in the plasma led to the heating of the particles and the increasing of the plasma temperature.

References

1.J. C. Metcalfe, and M. B. C. Quigley, Heat transfer in plasma-arc welding, Welding Journal 54,3 (1975) 99s-103s.
2.J. M. Dawson and J. Oberman. High frequency conductivity and the emission and absorption coefficients of a fully ionized plasma. Phys. Fluids, 5 (1962)517.
3.A. B. Langdon. Nonlinear inverse bremsstrahlung and heated electron distributions. Phys. Rev. Lett., 44 (1980)575 .
4.D. Forslund, J. Kindel, K. Lee, E. Lindman, and R. Morse. Theory and simulation of resonant absorption in a hot plasma. Phys. Rev. A, 11 (1975)679.
5.Yu. P. Bilokh, Plasmon mechanism of light transmission through a metal film or a plasma layer, Optics comm. 259(2006)436-444.
6.R. Dragila, B. Luther-Davies and S. Vukovic 1985 High transparency of classically opaque metallic films, *Physics Review Letter.* **55**, 1117–1120.
7.L. Rajaei, S. Miraboutalebi and B. Shokri 2011 Transmission of Electromagnetic wave Through a Warm Over-dense Plasma layer with dissipative factor, *Phys Scr.* **84**, 8949.
8.S. Miraboutalebi, L. Rajaei, and M. K. KhadiviBorogeni, Plasmon resonance coupling in cold overdense dissipative plasma, Journal of Theoretical and Applied Physics 7.1 (2013)1-9.
9.S. Miraboutalebi, L. Rajaee, and L. FarhangMatin, Surface wave excitations on magnetized over-dense plasma, Journal of Theoretical and Applied Physics 6.1 (2012)1-8.

Chaotic Modeling and Simulation (CMSIM) 2: 199-206, 2014

The Presence of Chaos in the GDP Growth Rate Time Series

Radko Kříž, Radka Kněžáčková

University of Pardubice, Czech Republic
E-mail: Radko.Kriz@upce.cz, Radka.Knezackova@upce.cz

Abstract: The goal of this paper is to find chaos in the Gross domestic product (GDP) growth rate of selected European countries. We chose only those European countries where data is available since 1980, because we needed the longest time series possible. These are the following states: Belgium, Finland, France, Norway, Spain, Switzerland and United Kingdom. At first we will estimate the time delay and the embedding dimension, which is needed for the largest Lyapunov exponent estimation. The largest Lyapunov exponent is one of the important indicators of chaos and is generally well-known. Subsequently we will calculate the 0-1 test for chaos. Finally we will compute the Hurst exponent by using the Rescaled Range analysis. The Hurst exponent is a numerical estimate of the predictability of a time series. The results indicated that chaotic behaviors obviously exist in GDP growth rate.
Keywords: Chaos theory, GDP, GDP growth rate, Time series analysis, Phase Space Reconstruction, Hurst exponent, largest Lyapunov exponent.

1. Introduction

Humanity has always been concerned with the question of whether the processes in the real world are deterministic in nature. Determinism can be understood variously. In this paper we assume a mathematical sense of determinism, which is given by equations and initial conditions. Mathematical models that are not deterministic because they involve randomness are called stochastic. Are the processes in the real world deterministic or stochastic in nature? Real processes in nature, according to the expectation of Mandelbrot [16], lie somewhere between pure deterministic process and white noise. This is why we can describe reality either by a stochastic or deterministic model. The Hurst coefficient can give us an answer to this.

An interesting case of determinism is deterministic chaos. The only purely stochastic process is a mathematical model described by mathematical statistics. The statistical model often works and is one of many possible descriptions if we do not know the system. This also applies to economic quantities, including forecasts for GDP. The basic question is therefore the existence of chaotic behavior. If the system behaves chaotically, we are forced to accept only limited predictions. In this paper we will try to show the chaotic behavior of GDP growth rate.

Received: 24 April 2013 / Accepted: 11 January 2014
© 2014 CMSIM
ISSN 2241-0503

2. Methods of analyzing

In short, we will describe the basic definitions and the basic methods for examining the input data.

2.1 Phase space reconstruction

According to Henry [9], the main goal in nonlinear time series analysis is to determine whether or not a given time series is of a deterministic nature. If it is, then further questions of interest are: What is the dimension of the phase space supporting the data set? Is the data set chaotic?

The key to answering these questions is embodied in the method of phase space reconstruction, which has been rigorously proven by the embedding theorems of Takens [19]. Takens theorem was independently suggested for example Packard [17]. Takens' theorem transforms the prediction problem from time extrapolation to phase space interpolation.

Let there be given a time series $x_1, x_2, \ldots, x_N$ which is embedded into the m-dimensional phase space by the time delay vectors. A point in the phase space is given as:

$$Y_n = x_n, x_{n-\tau}, \ldots, x_{n-(m-1)\tau} \quad n = 1,2,\ldots, N-(m-1)\tau \tag{1}$$

where τ is the time delay and m is the embedding dimension. Different choices of τ and m yield different reconstructed trajectories. How can we determine optimal τ and m?

2.2 Optimal time delay

A one-to-one embedding can be obtained for any value of the time delay $\tau > 0$. However, very small time delays will result in near-linear reconstructions with high correlations between consecutive phase space points and very large delays might obscure the deterministic structure linking points along a single degree of freedom. If the time delay is commensurate with a characteristic time in the underlying dynamics, then this too may result in a distorted reconstruction.

In order to estimate τ, two criteria are important according to Kodba [12]. First, τ has to be large enough so that the information we get from measuring the value of x at time $n + \tau$ is significantly different from the information we already have by knowing the value of x at time n. Only then will it be possible to gather enough information about all other system variables that influence the value of x to reconstruct the whole attractor. Second, τ should not be larger than the typical time in which the system loses memory of its initial state. This is particularly important for chaotic systems, which are intrinsically unpredictable and hence lose memory of the initial state as time progresses. [14]

Following this reasoning, Fraser and Swinney [3] introduced the mutual information between x_n and $x_{n+\tau}$ as a suitable quantity for determining τ. The mutual information between x_n and $x_{n+\tau}$ quantifies the amount of information we have about the state $x_{n+\tau}$ presuming we know the state x_n. Now we can define mutual information function:

$$I(\tau) = -\sum_{h=1}^{j}\sum_{k=1}^{j} P_{h,k}(\tau) \ln \frac{P_{h,k}(\tau)}{P_h P_k} \tag{2}$$

where P_h and P_k denote the probabilities that the variable assumes a value inside the h^{th} and k^{th} bins, respectively, and $P_{h,k}(\tau)$is the joint probability that x_n is in bin h and $x_{n+\tau}$ is in bin k. Hence, the first minimum of $I(\tau)$ marks the optimal choice for the time delay.

2.3 Optimal embedding dimension

The embedding dimension m is conventionally chosen using the "false nearest neighbors'" method. This method measures the percentage of close neighboring points in a given dimension that remain so in the next highest dimension. The minimum embedding dimension capable of containing the reconstructed attractor is that for which the percentage of false nearest neighbors drops to zero for a given tolerance level ε. [14]

In order to calculate the fraction of false nearest neighbors the following algorithm is used according to Kennel [11]. Given a point $p(i)$ in the m-dimensional embedding space, one first has to find a neighbour $p(j)$, so that

$$\left\| p(i) - p(j) \right\| \le \varepsilon \tag{3}$$

We then calculate the normalized distance R_i between the $(m + 1)th$ embedding coordinate of points $p(i)$ and $p(j)$ according to the equation:

$$R_i = \frac{\left| x_{i+m\tau} - x_{j+m\tau} \right|}{\left\| p(i) - p(j) \right\|} \tag{4}$$

If R_i is larger than a given threshold R_{tr} , then $p(i)$ is marked as having a false nearest neighbor. Equation (4) has to be applied for the whole time series and for various $m = 1, 2, \ldots$ until the fraction of points for which $R_i > R_{tr}$ is negligible [12].

2.4 The largest Lyapunov exponent

Lyapunov exponent λ of a dynamical system is a quantity that characterizes the rate of separation of infinitesimally close trajectories. Quantitatively, two trajectories in phase space with initial separation δZ_0 diverge.

$$\delta Z(t) \approx e^{\lambda t} \left| \delta Z_0 \right| \tag{5}$$

The largest Lyapunov exponent (LLE) can be defined as follows:

$$\lambda = \lim_{\substack{\delta Z_0 \to 0 \\ t \to \infty}} \frac{1}{t} \ln \frac{\left| \delta Z(t) \right|}{\left| \delta Z_0 \right|} \tag{6}$$

The limit $\delta Z0 \to 0$ ensures the validity of the linear approximation at any time. LLE determines a notion of predictability for a dynamical system. A positive LLE is usually taken as an indication that the system is chaotic (provided some other conditions are met, e.g., phase space compactness) [15].

We have used the Rosenstein algorithm, which counts the LLE as follows:

$$\lambda_1(i) = \frac{1}{i\Delta t} . \frac{1}{(M-i)} \sum_{j=1}^{M-i} \ln \frac{d_j(i)}{d_j(0)} \tag{7}$$

Where $d_j(i)$ is distance from the j point to its nearest neighbor after i time steps and M is the number of reconstructed points. For more information see [6, 18].

2.5 The 0-1 test for chaos

New test for the presence of deterministic chaos was developed by Gottwald & Melbourne [7]. Their '0 - 1 test for chaos takes as input a time series of measurements, and returns a single scalar value usually in the range 0 - 1. In contrast the 0 - 1 test does not depend on phase space reconstruction but rather works directly with the time series given. The input is the time-series data and the output is 0 or 1, depending on whether the dynamics is non-chaotic or chaotic.

Briefly, the 0-1 test takes as input a scalar time series of observations $\varphi_1, \ldots, \varphi_N$. We have used the algorithm according to Dawes & Freeland [1]. First, we must fix a real parameter c and construct the Fourier transformed series:

$$z_n = \sum_{j=1}^{n} \phi_j e^{ijc}, \quad n = 1,\ldots,N \tag{8}$$

Then we have computed the smoothed mean square displacement:

$$M_c(n) = \frac{1}{N-p}\sum_{j=1}^{N-p}\left|z_{j+n} - z_j\right|^2 - \left(\sum_{k=1}^{N}\frac{\phi_k}{N}\right)^2 \frac{1-\cos nc}{1-\cos c} \tag{9}$$

Finally we have estimated correlation coefficient to evaluate the strength of the linear growth

$$r_c = \frac{\operatorname{cov}(n, M_c(n))}{\sqrt{\operatorname{cov}(n,n)\operatorname{cov}(M_c(n), M_c(n))}} \tag{10}$$

2.6 Long memory in time series

Hurst exponent (H) is widely used to characterize some processes. Hurst exponent is used to evaluate the presence or absence of long-range dependence and its degree in a time-series. For more information see [8, 10]. The Hurst exponent is a measure that has been widely used to evaluate the self-similarity and correlation properties of fractional Brownian noise, the time series produced by a fractional Gaussian process [16]. We can describe self-similarity process following equation:

$$X(at) = a^H X(t) \tag{11}$$

where a is a positive constant, and H is the self-similarity parameter, for $0 < H < 1$.

We have used a methodology known as Rescaled Range analysis or R/S analysis. To calculate the Hurst exponent, one must estimate the dependence of the rescaled range on the time span n of observation. The Hurst exponent is defined in terms of the asymptotic behavior of the rescaled range as a function of the time span of a time series as follows:

$$E\left[\frac{R(n)}{S(n)}\right] = Cn^H \text{ as } n \to \infty \quad (12)$$

Where *[R(n)/S(n)]* is the rescaled range; *E[y]* is expected value; *n* is number of data points in a time series, *C* is a constant. For more information see [13].

3. Analysis of GDP growth rate time series

3.1 Input data

The GDP in current prices in millions of national currency (including 'euro fixed' series for euro area countries) is used in this paper. We have used data (quarterly, seasonally adjusted and adjusted data by working days) from the Eurostat between the years 1980 - 2012. According to Eurostat [2], seasonal adjustment is a treatment of infra-annual time series to remove the spurious effect of seasonal patterns from the series' trend and cycle. These patterns can be caused by weather, public holidays such as Christmas, the timing of school vacations or of dividend payments and a number of other reasons.

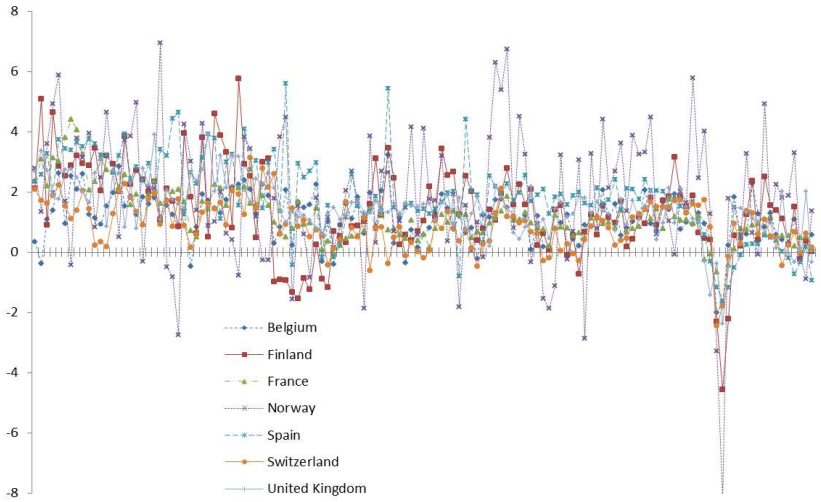

Fig. 1. GDP growth rate time series.

Generally, the main problem in analyzing the GDP time series is the lack of data. That is why we chose only those European countries where data is available since 1980. These are the following states: Belgium, Finland, France, Norway, Spain, Switzerland and United Kingdom. So, we have 132 values from these countries. The analysis of such short time series in the context of nonlinear dynamics or in the presence of chaos can be questionable. We know, according to Horák [4] or Galka [5], that for this kind of method results are provable for at least 10^3 data-points. Analysis of short time series (order of 10^1) may lead to a spurious estimation of the invariants e.g. LLE. Despite the above, we have no choice but to analyze GDP time series in the context of nonlinear dynamics and try to find chaotic behavior of GDP growth rate time series. Therefore, all

results are only estimates. The second problem can be the presence of trends in time series. Trended data are not suitable for future analysis to study chaos dynamics. There is no universal way to remove the trend from the data set. The results often depend strongly on how the data are detrended. This is solved using the GDP growth rate (cf. Figure 1).

3.2 Calculation of the largest Lyapunov exponents

At first we will estimate the time delay and the embedding dimension, which is needed for the largest Lyapunov exponent estimation. We will use the mutual information approach to determine the time delay. The first minimum of the mutual information function $I(\tau)$ (2) marks the optimal choice for the time delay. The embedding dimension m is chosen using the "false nearest neighbors'" method. The minimum embedding dimension capable of containing the reconstructed attractor is that for which the percentage of false nearest neighbors drops to zero for a given tolerance level ε. Then, we calculated the LLE using the Rosenstein algorithm. All computed values are positive (cf. Figure 2). A positive LLE is usually taken as an indication that the system is chaotic.

	Tau	ED	LLE	H	test 0- 1
Belgium	2	3	0,032	0,76	0,99
Finland	3	3	0,840	0,88	0,99
France	3	3	0,084	0,96	0,82
Norway	1	3	0,011	0,54	0,99
Spain	2	3	0,078	0,99	0,95
Switzerland	3	3	0,585	0,82	0,99
United Kingdom	4	3	0,071	0,96	0,98
Average	2,571	3,000	0,243	0,844	0,959
SD	0,904	0,000	0,306	0,146	0,058

Fig. 2. The optimal time delay, The optimal embedding dimension, The Largest Lyapunov exponent, The Hurst exponent, Value of chaos test 0-1 for selected countries, average and standard deviation

3.3 Results of the 0-1 Test for Chaos

In this chapter we calculate the correlation coefficient as was shown above. The correlation coefficient is near to 0 for non-chaotic data and near 1 for chaotic data. All computed values are very close to 1 (cf. Figure 2). Hence, we can convincingly assume there to be chaotic behavior in the GDP growth rate time series.

3.4 Calculation of the Hurst exponent

The Rescaled Range analysis gave us values of the Hurst exponent between 0,54 (Norway) and 0,99 (Spain) (cf. Figure 2). Most values indicate the presence of long memory in GDP growth rate time series except the value of the Hurst

exponent for the Norway GDP growth rate, which indicates random walk. Those values are in accordance with our expectations. We know that the value of H is between 0 and 1, whilst real time series are usually higher than 0,5. If the exponent value is close to 0 or 1, it means that the time-series has long-range dependence. We can assume that the true value lies somewhere between those values. We think that those values are sufficient for a credible prediction. Now we also know that the fractal dimension DF =2-H. We have estimated the values of the fractal dimension selected time series between 1,01 and 1,46.

4. Conclusions

Chaos theory has changed the thinking of scientists and the methodology of science. Making a theoretical prediction and then matching it to the experiment is not possible in chaotic processes. Long term forecasts are, in principle, also impossible according to chaos theory. The main problem is in the quantity and quality of data. Some improvement of measurement cannot help us adequately, because it is a fight against power of exponential rate. Nonlinear dynamics and chaos theory have also corrected the old reductionist tendency in science. Now it is known that real processes are nonlinear and a linear view can be wrong. The basic question is therefore - the existence of chaotic behavior. If the system behaves chaotically, we are forced to accept only limited predictions. But it is much better than random processes.

Although we analyzed various GDP growth rate time series, the results came out very similar. We have shown in this paper that the GDP growth rate time series are chaotic and contain long memory. First, we computed the values of the time delays and the embedding dimensions. The average value of computed time delays is 2,6. In all 7 cases we chose the value 3 as the optimal embedding dimension. Subsequently, we calculated the LLE and all computed values were positive. A positive LLE is usually taken as an indication that the system is chaotic. If the fractal dimension is low, the LLE is positive and the Kolmogorov entropy has a finite positive value, chaos is probably present. Then we conducted the 0-1 test for chaos according to which chaos was present. All computed values were very close to 1. Hence, we can convincingly assume there to be chaotic behavior in the GDP growth rate time series. From these estimations it can be concluded that the GDP growth rate time series is chaotic. Finally we have computed the Hurst exponent by Rescaled Range analysis. Most values indicate the presence of long memory in GDP growth rate time series, except the value for the Norway GDP growth rate.

We know that the main problem when analyzing GDP time series is the lack of data. As mentioned above, we chose only those European countries where data is available since 1980. Although these time series are not ideal in length, they are acceptable for analysis. The results came out mostly very similar. The presence of chaos in selected GDP growth time series is not only a coincidence.

In the future we would like to focus on the proper statistical significance for nonlinearity and on predicting the GDP. In particular, the surrogate data approach (e.g. Theiler et al. [20]) is a powerful tool for detecting actual nonlinear behavior, and distinguishing it from other phenomena.

References

[1] DAWES, J., H., P., FREELAND, M., C.: The '0–1 test for chaos' and strange nonchaotic attractors, people.bath.ac.uk/jhpd20/publications, 2008.

[2] ESS Handbook for Quality Reports, Luxembourg: Office for Official Publications of the European Communities, 2009

[3] FRASER, A., M., SWINNEY, H., L.: Independent coordinates for strange attractors from mutual information Phys. Rev. A 33 1134–40, 1986.

[4] HORÁK, J., KRLÍN, L., RAIDL, A.,: Deterministický chaos a jeho fyzikální aplikace, Academia, Praha, 437, 2003.

[5] GALKA, A.,: Topics in Nonlinear Time Series Analysis, World Scientific, (2000)

[6] GOTTHANS, T.,: Advanced algorithms for the analysis of data sequences in Matlab, Master's Thesis, University of technology Brno, 2010.

[7] GOTTWALD, G., A., MELBOURNE, I.,: A new test for chaos in deterministic systems. Proc. Roy. Soc. A 460 603–611, 2004.

[8] GRASSBERG, P, PROCACCIA, I, Characterization of strange attractors, Phys. Rev. Lett. 50, 346, 1983.

[9] HENRY, B., LOVELL, N., CAMACHO, F.,: Nonlinear dynamics time series analysis, in Akay,M. (ed.), Nonlinear Biomedical Signal Processing, Insititue of Electrical and Electronics Engineers, Inc., pp. 1 – 39, 2001.

[10] HURST, H., E.,: "Long term storage capacity of reservoirs". Trans. Am. Soc. Eng. 116: 770–799, 1951.

[11] KENNEL, M., B., BROWN, R., ABARBANEL, H., D., I.,: Determining embedding dimension for phase space reconstruction using a geometrical construction Phys. Rev. A 45 3403–11, 1992.

[12] KODBA, S., PERC, M., MARHL, M.,: Detecting chaos from a time series. European Journal of Physics 26, 205–215, 2005.

[13] KŘÍŽ, R,: Chaos in GDP, Acta Polytechnica Vol. 51 No. 5, 2011.

[14] KŘÍŽ, R.: Chaotic Analysis of the GDP Time Series, In: Nostradamus 2013: Prediction, Modeling and Analysis of Complex Systems, vol. 210, Springer International Publishing, 2013, pp. 353–362.

[15] LORENZ, H-W.,: Nonlinear Dynamical Economics and Chaotic Motion, Springer-Verlag, 1989.

[16] MANDELBROT, B., B.,: The Fractal Geometry of Nature, W.H. Freeman and Co., 1983.

[17] PACKARD, N., H., CRUTCHFIELD, J., P., FARMER, J., D., SHAW, R., S.,: Geometry from a time series. Phys Rev Lett 1980; 45:712–6.

[18] ROSENSTEIN, M., T., COLLINS J., J., LUCA, C., J.,: A practical method for calculating largest Lyapunov exponents from small data sets. Physica D 65:117-134, 1993.

[19] TAKENS, F.,: Detecting Strange Attractor in Turbulence (Lecture Notes in Mathematics vol 898) ed D A Rand and L S Young (Berlin: Springer) p 366, 1981.

[20] THEILER, J., EUBANK, J., LONGTIN, A., GALDRIKIAN, B., FARMER J., D.,: Testing for nonlinearity in time series: The method of surrogate data, Physica D 58, 77 (1992)